The Astrophysical Journal, 721:1425–1447, 2010 October 1 doi:10.1088/0004-637X/721/2/1425

FERMI LARGE AREA TELESCOPE AND MULTI-WAVELENGTH OBSERVATIONS OF THE FLARING ACTIVITY OF PKS 1510-089 BETWEEN 2008 SEPTEMBER AND 2009 JUNE

A. A. Abdo[1,2,79], M. Ackermann[3], I. Agudo[4,5], M. Ajello[3], A. Allafort[3], H. D. Aller[6], M. F. Aller[6], E. Antolini[7,8], A. A. Arkharov[9], M. Axelsson[10,11,12], U. Bach[13], L. Baldini[14], J. Ballet[15], G. Barbiellini[16,17], D. Bastieri[18,19], K. Bechtol[3], R. Bellazzini[14], A. Berdyugin[20], B. Berenji[3], R. D. Blandford[3], D. A. Blinov[21], E. D. Bloom[3], M. Boettcher[22], E. Bonamente[7,8], A. W. Borgland[3], A. Bouvier[3], J. Bregeon[14], A. Brez[14], M. Brigida[23,24], P. Bruel[25], R. Buehler[3], C. S. Buemi[26], T. H. Burnett[27], S. Buson[18,19], G. A. Caliandro[28], R. A. Cameron[3], P. A. Caraveo[29], D. Carosati[30], S. Carrigan[19], J. M. Casandjian[15], E. Cavazzuti[31], C. Cecchi[7,8], Ö. Çelik[32,33,34], A. Chekhtman[1,35], W. P. Chen[36], C. C. Cheung[1,2], J. Chiang[3], S. Ciprini[8], R. Claus[3], J. Cohen-Tanugi[37], J. Conrad[12,38,80], S. Corbel[15,39], L. Costamante[3], C. D. Dermer[1], A. de Angelis[40], F. de Palma[23,24], D. Donato[32], E. do Couto e Silva[3], P. S. Drell[3], R. Dubois[3], D. Dumora[41,42], C. Farnier[37], C. Favuzzi[23,24], S. J. Fegan[25], E. C. Ferrara[32], W. B. Focke[3], E. Forné[43], P. Fortin[25], Y. Fukazawa[44], S. Funk[3], P. Fusco[23,24], F. Gargano[24], D. Gasparrini[31], N. Gehrels[32], S. Germani[7,8], B. Giebels[25], N. Giglietto[23,24], F. Giordano[23,24], M. Giroletti[45], T. Glanzman[3], G. Godfrey[3], I. A. Grenier[15], J. E. Grove[1], S. Guiriec[46], M. A. Gurwell[47], C. Gusbar[22], J. L. Gómez[4], D. Hadasch[48], V. A. Hagen-Thorn[21,49], M. Hayashida[3], E. Hays[32], D. Horan[25], R. E. Hughes[50], G. Jóhannesson[3], A. S. Johnson[3], W. N. Johnson[1], T. Kamae[3], H. Katagiri[44], J. Kataoka[51], N. Kawai[52,53], G. Kimeridze[54], J. Knödlseder[55], T. S. Konstantinova[21], E. N. Kopatskaya[21], E. Koptelova[36], Y. Y. Kovalev[13,56], O. M. Kurtanidze[54], M. Kuss[14], A. Lahteenmaki[57], J. Lande[3], V. M. Larionov[9,21,49], E. G. Larionova[21], L. V. Larionova[21], S. Larsson[10,12,38], L. Latronico[14], S.-H. Lee[3], P. Leto[26], M. L. Lister[58], F. Longo[16,17], F. Loparco[23,24], B. Lott[41,42], M. N. Lovellette[1], P. Lubrano[7,8], G. M. Madejski[3], A. Makeev[1,35], E. Massaro[59], M. N. Mazziotta[24], W. McConville[32,60], J. E. McEnery[32,60], I. M. McHardy[61], P. F. Michelson[3], W. Mitthumsiri[3], T. Mizuno[44], A. A. Moiseev[33,60], C. Monte[23,24], M. E. Monzani[3], D. A. Morozova[21], A. Morselli[62], I. V. Moskalenko[3], S. Murgia[3], M. Naumann-Godo[15], M. G. Nikolashvili[21], P. L. Nolan[3], J. P. Norris[63], E. Nuss[37], M. Ohno[64], T. Ohsugi[65], A. Okumura[64], N. Omodei[3], E. Orlando[66], J. F. Ormes[63], M. Ozaki[64], D. Paneque[3], J. H. Panetta[3], D. Parent[1,35], M. Pasanen[20], V. Pelassa[37], M. Pepe[7,8], M. Pesce-Rollins[14], F. Piron[37], T. A. Porter[3], A. B. Pushkarev[9,13,67], S. Rainò[23,24], C. M. Raiteri[68], R. Rando[18,19], M. Razzano[14], A. Reimer[3,69], O. Reimer[3,69], R. Reinthal[20], J. Ripken[12,38], S. Ritz[70], M. Roca-Sogorb[4], A. Y. Rodriguez[28], M. Roth[27], P. Roustazadeh[22], F. Ryde[12,71], H. F.-W. Sadrozinski[70], A. Sander[50], J. D. Scargle[72], C. Sgrò[14], L. A. Sigua[54], P. D. Smith[50], K. Sokolovsky[13,56], G. Spandre[14], P. Spinelli[23,24], J.-L. Starck[15], M. S. Strickman[1], D. J. Suson[73], H. Takahashi[65], T. Takahashi[64], L. O. Takalo[20], T. Tanaka[3], B. Taylor[74], J. B. Thayer[3], J. G. Thayer[3], D. J. Thompson[32], L. Tibaldo[15,18,19,81], M. Tornikoski[57], D. F. Torres[28,48], G. Tosti[7,8], A. Tramacere[3,75,76], C. Trigilio[26], I. S. Troitsky[21], G. Umana[26], T. L. Usher[3], J. Vandenbroucke[3], V. Vasileiou[33,34], N. Vilchez[55], M. Villata[68], V. Vitale[62,77], A. P. Waite[3], P. Wang[3], B. L. Winer[50], K. S. Wood[1], Z. Yang[12,38], T. Ylinen[12,71,78], and M. Ziegler[70]

[1] Space Science Division, Naval Research Laboratory, Washington, DC 20375, USA
[2] National Academy of Sciences, Washington, DC 20001, USA
[3] W. W. Hansen Experimental Physics Laboratory, Kavli Institute for Particle Astrophysics and Cosmology, Department of Physics and SLAC National Accelerator Laboratory, Stanford University, Stanford, CA 94305, USA; tramacer@slac.stanford.edu
[4] Instituto de Astrofísica de Andalucía, CSIC, Apdo. 3004, Granada 18080, Spain
[5] Institute for Astrophysical Research, Boston University, Boston, MA 02215, USA
[6] Department of Astronomy, University of Michigan, Ann Arbor, MI 48109-1042, USA
[7] Istituto Nazionale di Fisica Nucleare, Sezione di Perugia, I-06123 Perugia, Italy
[8] Dipartimento di Fisica, Università degli Studi di Perugia, I-06123 Perugia, Italy
[9] Pulkovo Observatory, 196140 St. Petersburg, Russia
[10] Department of Astronomy, Stockholm University, SE-106 91 Stockholm, Sweden
[11] Lund Observatory, SE-221 00 Lund, Sweden
[12] The Oskar Klein Centre for Cosmoparticle Physics, AlbaNova, SE-106 91 Stockholm, Sweden
[13] Max-Planck-Institut für Radioastronomie, Auf dem Hügel 69, 53121 Bonn, Germany
[14] Istituto Nazionale di Fisica Nucleare, Sezione di Pisa, I-56127 Pisa, Italy
[15] Laboratoire AIM, CEA-IRFU/CNRS/Université Paris Diderot, Service d'Astrophysique, CEA Saclay, 91191 Gif sur Yvette, France
[16] Istituto Nazionale di Fisica Nucleare, Sezione di Trieste, I-34127 Trieste, Italy
[17] Dipartimento di Fisica, Università di Trieste, I-34127 Trieste, Italy
[18] Istituto Nazionale di Fisica Nucleare, Sezione di Padova, I-35131 Padova, Italy
[19] Dipartimento di Fisica "G. Galilei," Università di Padova, I-35131 Padova, Italy
[20] Tuorla Observatory, University of Turku, FI-21500 Piikkiö, Finland
[21] Astronomical Institute, St. Petersburg State University, St. Petersburg, Russia
[22] Department of Physics and Astronomy, Ohio University, Athens, OH 45701, USA
[23] Dipartimento di Fisica "M. Merlin" dell'Università e del Politecnico di Bari, I-70126 Bari, Italy
[24] Istituto Nazionale di Fisica Nucleare, Sezione di Bari, 70126 Bari, Italy
[25] Laboratoire Leprince-Ringuet, École polytechnique, CNRS/IN2P3, Palaiseau, France
[26] Osservatorio Astrofisico di Catania, 95123 Catania, Italy
[27] Department of Physics, University of Washington, Seattle, WA 98195-1560, USA
[28] Institut de Ciencies de l'Espai (IEEC-CSIC), Campus UAB, 08193 Barcelona, Spain
[29] INAF-Istituto di Astrofisica Spaziale e Fisica Cosmica, I-20133 Milano, Italy
[30] EPT Observatories, Tijarafe, La Palma, Spain

[31] Agenzia Spaziale Italiana (ASI) Science Data Center, I-00044 Frascati (Roma), Italy
[32] NASA Goddard Space Flight Center, Greenbelt, MD 20771, USA
[33] Center for Research and Exploration in Space Science and Technology (CRESST) and NASA Goddard Space Flight Center, Greenbelt, MD 20771, USA
[34] Department of Physics and Center for Space Sciences and Technology, University of Maryland Baltimore County, Baltimore, MD 21250, USA
[35] George Mason University, Fairfax, VA 22030, USA
[36] Graduate Institute of Astronomy, National Central University, Jhongli 32054, Taiwan
[37] Laboratoire de Physique Théorique et Astroparticules, Université Montpellier 2, CNRS/IN2P3, Montpellier, France
[38] Department of Physics, Stockholm University, AlbaNova, SE-106 91 Stockholm, Sweden
[39] Institut universitaire de France, 75005 Paris, France
[40] Dipartimento di Fisica, Università di Udine and Istituto Nazionale di Fisica Nucleare, Sezione di Trieste, Gruppo Collegato di Udine, I-33100 Udine, Italy
[41] CNRS/IN2P3, Centre d'Études Nucléaires Bordeaux Gradignan, UMR 5797, Gradignan, 33175, France
[42] Université de Bordeaux, Centre d'Études Nucléaires Bordeaux Gradignan, UMR 5797, Gradignan, 33175, France
[43] Agrupació Astronòmica de Sabadell, 08206 Sabadell, Spain
[44] Department of Physical Sciences, Hiroshima University, Higashi-Hiroshima, Hiroshima 739-8526, Japan
[45] INAF Istituto di Radioastronomia, 40129 Bologna, Italy
[46] Center for Space Plasma and Aeronomic Research (CSPAR), University of Alabama in Huntsville, Huntsville, AL 35899, USA
[47] Harvard-Smithsonian Center for Astrophysics, Cambridge, MA 02138, USA
[48] Institució Catalana de Recerca i Estudis Avançats (ICREA), Barcelona, Spain
[49] Isaac Newton Institute of Chile, St. Petersburg Branch, St. Petersburg, Russia
[50] Department of Physics, Center for Cosmology and Astro-Particle Physics, The Ohio State University, Columbus, OH 43210, USA
[51] Research Institute for Science and Engineering, Waseda University, 3-4-1, Okubo, Shinjuku, Tokyo 169-8555, Japan
[52] Department of Physics, Tokyo Institute of Technology, Meguro City, Tokyo 152-8551, Japan
[53] Cosmic Radiation Laboratory, Institute of Physical and Chemical Research (RIKEN), Wako, Saitama 351-0198, Japan
[54] Abastumani Observatory, Mt. Kanobili, 0301 Abastumani, Georgia
[55] Centre d'Étude Spatiale des Rayonnements, CNRS/UPS, BP 44346, F-30128 Toulouse Cedex 4, France
[56] Astro Space Center of the Lebedev Physical Institute, 117810 Moscow, Russia
[57] Metsähovi Radio Observatory, Helsinki University of Technology TKK, FIN-02540 Kylmala, Finland
[58] Department of Physics, Purdue University, West Lafayette, IN 47907, USA
[59] Physics Department, Università di Roma "La Sapienza," I-00185 Roma, Italy; enrico.massaro@uniroma1.it
[60] Department of Physics and Department of Astronomy, University of Maryland, College Park, MD 20742, USA
[61] School of Physics and Astronomy, University of Southampton, Highfield, Southampton, SO17 1BJ, UK
[62] Istituto Nazionale di Fisica Nucleare, Sezione di Roma "Tor Vergata," I-00133 Roma, Italy
[63] Department of Physics and Astronomy, University of Denver, Denver, CO 80208, USA
[64] Institute of Space and Astronautical Science, JAXA, 3-1-1 Yoshinodai, Sagamihara, Kanagawa 229-8510, Japan
[65] Hiroshima Astrophysical Science Center, Hiroshima University, Higashi-Hiroshima, Hiroshima 739-8526, Japan
[66] Max-Planck Institut für extraterrestrische Physik, 85748 Garching, Germany
[67] Crimean Astrophysical Observatory, 98409 Nauchny, Crimea, Ukraine
[68] INAF, Osservatorio Astronomico di Torino, I-10025 Pino Torinese (TO), Italy
[69] Institut für Astro- und Teilchenphysik and Institut für Theoretische Physik, Leopold-Franzens-Universität Innsbruck, A-6020 Innsbruck, Austria
[70] Santa Cruz Institute for Particle Physics, Department of Physics and Department of Astronomy and Astrophysics, University of California at Santa Cruz, Santa Cruz, CA 95064, USA
[71] Department of Physics, Royal Institute of Technology (KTH), AlbaNova, SE-106 91 Stockholm, Sweden
[72] Space Sciences Division, NASA Ames Research Center, Moffett Field, CA 94035-1000, USA
[73] Department of Chemistry and Physics, Purdue University Calumet, Hammond, IN 46323-2094, USA
[74] Lowell Observatory, Flagstaff, AZ 86001, USA
[75] Consorzio Interuniversitario per la Fisica Spaziale (CIFS), I-10133 Torino, Italy
[76] INTEGRAL Science Data Centre, CH-1290 Versoix, Switzerland
[77] Dipartimento di Fisica, Università di Roma "Tor Vergata," I-00133 Roma, Italy
[78] School of Pure and Applied Natural Sciences, University of Kalmar, SE-391 82 Kalmar, Sweden
Received 2010 April 30; accepted 2010 July 2; published 2010 September 10

ABSTRACT

We report on the multi-wavelength observations of PKS 1510-089 (a flat spectrum radio quasar (FSRQ) at $z = 0.361$) during its high activity period between 2008 September and 2009 June. During this 11 month period, the source was characterized by a complex variability at optical, UV, and γ-ray bands, on timescales down to 6–12 hr. The brightest γ-ray isotropic luminosity, recorded on 2009 March 26, was $\simeq 2 \times 10^{48}$ erg s^{-1}. The spectrum in the *Fermi* Large Area Telescope energy range shows a mild curvature described well by a log-parabolic law, and can be understood as due to the Klein–Nishina effect. The γ-ray flux has a complex correlation with the other wavelengths. There is no correlation at all with the X-ray band, a weak correlation with the UV, and a significant correlation with the optical flux. The γ-ray flux seems to lead the optical one by about 13 days. From the UV photometry, we estimated a black hole mass of $\simeq 5.4 \times 10^8\ M_\odot$ and an accretion rate of $\simeq 0.5\ M_\odot$ yr^{-1}. Although the power in the thermal and non-thermal outputs is smaller compared to the very luminous and distant FSRQs, PKS 1510-089 exhibits a quite large Compton dominance and a prominent big blue bump (BBB) as observed in the most powerful γ-ray quasars. The BBB was still prominent during the historical maximum optical state in 2009 May, but the optical/UV spectral index was softer than in the quiescent state. This seems to indicate that the BBB was not completely dominated by the synchrotron emission during the highest optical state. We model the broadband spectrum assuming a leptonic scenario in which the inverse Compton emission is dominated by the scattering of soft photons produced externally to the jet. The resulting model-dependent jet energetic content is compatible with a scenario in which the jet is powered by the accretion disk, with a total efficiency within the Kerr black hole limit.

Key words: galaxies: active – galaxies: jets – gamma rays: galaxies – quasars: individual (PKS 1510-089)

Online-only material: color figures

1. INTRODUCTION

Among blazars, flat spectrum radio quasars (FSRQs) are those objects characterized by prominent emission lines in the optical spectra. The typical spectral energy distribution (SED) of blazars has a two bump shape. According to current models, the low-energy bump is interpreted as synchrotron emission from highly relativistic electrons, and the high-energy bump is interpreted as inverse Compton (IC) emission. In FSRQs, the IC bump can dominate over the synchrotron one by more than an order of magnitude. It is widely believed that in these sources the IC component is dominated by the scattering of soft photons produced externally to the jet (Sikora et al. 1994; Dermer & Schlickeiser 2002), rather than by the synchrotron self-Compton (SSC) emission (Jones et al. 1974; Ghisellini & Maraschi 1989). In the external radiation Compton (ERC) scenario, the seed photons for the IC process are typically UV photons generated by the accretion disk surrounding the black hole (BH), and reflected toward the jet by the broad line region (BLR) within a typical distance from the disk in the subparsec scale. If the emission occurs at larger distances, the external radiation is likely to be provided by a dusty torus (DT; Sikora et al. 2002). In this case, the radiation is typically peaked at IR frequencies.

The study of the SEDs of blazars and their complex variability has been greatly enriched since the 2008 August start of scientific observations by the Large Area Telescope (LAT; Atwood et al. 2009) on the *Fermi Gamma-ray Space Telescope* (Ritz 2007), thanks to its high sensitivity and survey mode.

One of the most active blazars observed in this period was the FSRQ PKS 1510-089. This object has an optical spectrum characterized by prominent emission lines overlying a blue continuum (Tadhunter et al. 1993) at a redshift $z = 0.361$ (Thompson et al. 1990). Radio images show a bright core with a jet that has a large misalignment between the arcsecond and milliarcsecond scales; superluminal velocity up to $\simeq 20c$ are also reported (Homan et al. 2002).

PKS 1510-089 was already detected in γ-rays by EGRET (Hartman et al. 1999) and exhibited a very interesting activity at all wavelengths. It was also detected by *AGILE* during 10 days of pointed observations from 2007 August 23 to 2007 September 1 (Pucella et al. 2008). In the period 2008–2009, PKS 1510-089 was observed to be bright and highly variable in several frequency bands. In gamma rays, it was detected in 2008 March by *AGILE* (D'Ammando et al. 2008) and other bright phases were observed in the subsequent months by both *Fermi*-LAT and *AGILE* (Tramacere 2008; Ciprini & Corbel 2009; D'Ammando et al. 2009b; Pucella et al. 2009; Vercellone et al. 2009; Cutini & Hays 2009). High states in X-rays and in optical were reported by Krimm et al. (2009), Villata et al. (2009a), and Larionov et al. (2009a, 2009b). In a recent paper, Marscher et al. (2010a) presented data from a multi-wavelength (MW) campaign concerning the same flaring period of PKS 1510-089. In that paper, the authors focus on analysis of the parsec-scale behavior and correlation of rotation of the optical polarization angle with the dramatic γ-ray activity.

In the present paper, we describe the results of the LAT monitoring together with the related MW campaigns covering the entire electromagnetic spectrum. We present a detailed analysis of the γ-ray spectral shape and spectral evolution, and of the MW SED modeling and interpretation. This paper is organized as follows: in Section 2, we report results on the γ-ray observation of PKS 1510-089 and we study the spectral shape and its evolution. In Section 3, we summarize multifrequency data obtained through simultaneous optical–UV–X-ray *Swift* observations and radio–optical observatories. In Section 4, we present the results of the multifrequency data and their connection with the γ-ray activity. In Section 5, we report our conclusions about the MW data, and we use a phenomenological analysis to estimate some of the physical fundamental parameters, such as the BH mass, the accretion disk bolometric luminosity, the shape of the electron distribution, and the beaming factor. We then model the observed SEDs and comment on the jet energetics. Furthermore, we compare PKS 1510-089 with other powerful FSRQs observed by *Fermi*. In Section 6, our final remarks are reported.

In the following, we use a ΛCDM (concordance) cosmology with values given within 1σ of the *Wilkinson Microwave Anisotropy Probe* (*WMAP*) results (Komatsu et al. 2009), namely, $h = 0.71$, $\Omega_m = 0.27$, and $\Omega_\Lambda = 0.73$, and a Hubble constant value $H_0 = 100\,h$ km s^{-1} Mpc^{-1}, the corresponding luminosity distance (d_L) is $\simeq 1.91$ Gpc ($\simeq 5.9 \times 10^{27}$ cm).

2. *FERMI*-LAT DATA AND RESULTS

The LAT data presented here were collected from 2008 August 4 to 2009 July 1. Only events with energies greater than 200 MeV were selected to minimize the systematic uncertainties. To have the highest probability that collected events are photons, the *diffuse* class selection was applied. A further selection on the zenith angle $>105^\circ$ was applied to avoid contamination from limb gamma rays. The analysis was performed using the Science Tools package[82] (v9r15p5). The instrument response functions (IRFs) P6_V3_DIFFUSE were used. These IRFs provide a correction for the pile-up effect. To produce light curves and spectral analysis the standard tool `gtlike` was used. The photons were extracted from a region of interest (ROI) centered on the source, within a radius of 7°. The `gtlike` model includes the PKS 1510-089 point source component and all the point sources form the first LAT catalog (Abdo et al. 2010a) that fall within 12° from the source. The model also includes a background component of the Galactic diffuse emission and an isotropic component, both of which are the standard models available from the *Fermi* Science Support Center[83] (FSSC). The isotropic component includes both contribution from the extragalactic diffuse emission and from the residual charged particle backgrounds. The estimated systematic uncertainty of the flux is 10% at 100 MeV, 5% at 500 MeV, and 20% at 10 GeV.

2.1. Temporal Behavior

We extracted light curves from the entire data set, to investigate the flaring activity. To take into account possible biases or systematics when the source flux is faint, we used two different time binnings of 1 day and 1 week. The light curves were extracted using `gtlike`, fitting the source spectrum by means of a power-law (PL) distribution ($dN/dE \propto E^{-\alpha_\gamma}$), where α_γ is the photon index, following the prescription given in the previous section. The flux was evaluated by integrating the fitted model above 0.2 GeV. The lower panel of Figure 1 clearly

[79] National Research Council Research Associate

[80] Royal Swedish Academy of Sciences Research Fellow, funded by a grant from the K. A. Wallenberg Foundation.

[81] Partially supported by the International Doctorate on Astroparticle Physics (IDAPP) program.

[82] http://fermi.gsfc.nasa.gov/ssc/data/analysis/documentation/Cicerone/

[83] http://fermi.gsfc.nasa.gov/ssc/data/access/lat/BackgroundModels.html

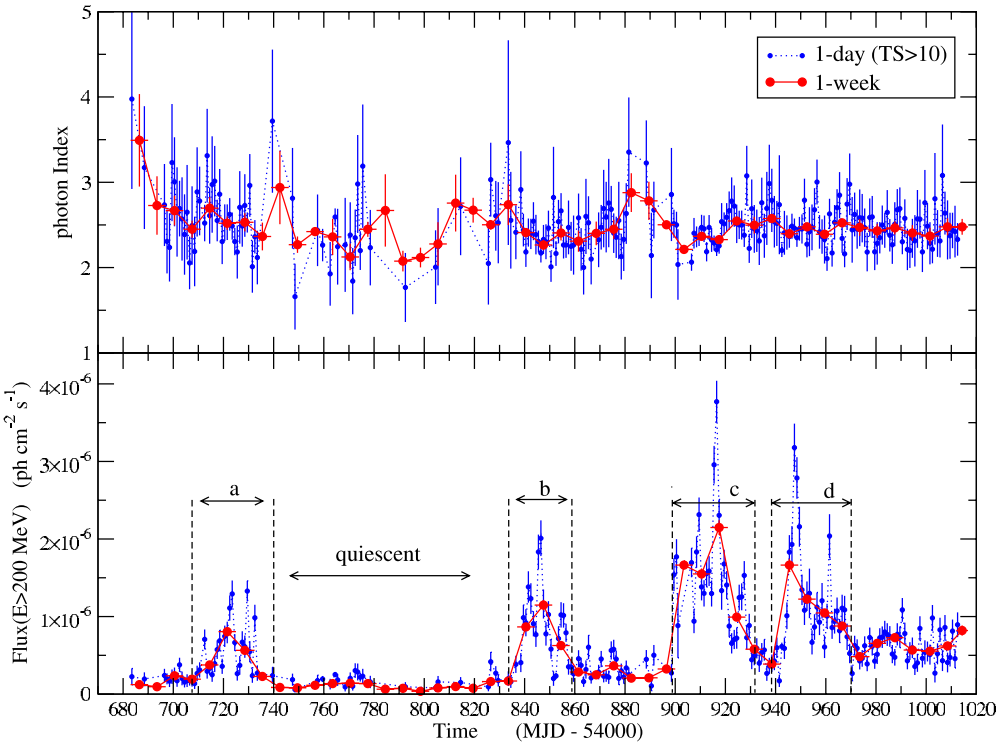

Figure 1. Upper panel: the γ-ray photon index (α_γ), as a function of time, for weekly and daily binning. In the case of daily binning, only observations with a test statistic > 10 are taken into account. The test statistic is defined as TS $= -2\log(L0/L1)$, where $L1$ and $L0$ are the likelihood of whether the source is included or not. Lower panel: light curves of weekly and daily (TS > 10) fluxes.

(A color version of this figure is available in the online journal.)

Table 1
Flaring Activity of PKS 1510-089 from 2008 August Until 2009 June

Source State	Start Date	Stop Date	Start MJD	Stop MJD
Flare a	2008 Aug 30	2008 Sep 26	54708	54735
Quiescent	2009 Sep 30	2010 Jan 1	54739	54832
Flare b	2009 Jan 4	2009 Jan 27	54835	54858
Flare c	2009 Mar 10	2009 Apr 9	54900	54930
Flare d	2009 Apr 15	2009 May 12	54936	54963

shows four major flaring episodes: between 2008 August 30 and 2008 September 26 (flare a), between 2009 January 4 and 2009 January 27 (flare b), between 2009 March 10 and 2009 April 9 (flare c), and between 2009 April 15 and 2009 May 12 (flare d). The source was almost quiescent between the end of 2008 September and the beginning of 2009 January (see Table 1 for a summary). The flux light curves with different temporal binning are compatible, with the daily integration binning showing better rapid flux variations that are smoothed in the weekly binning. A study of these variations based on the autocorrelation, Fourier analysis, and structure function is presented by Abdo et al. (2010d) together with other blazars.

Figure 2 shows close-up light curves of the four flares and the green line represents the optical data in the R filter (see Sections 3 and 4). Since the statistics during the flares were high, it was possible to use also a 12 hr binning (blue points). Typically, the flares have a complex structure with peaks having durations from about 1 to 5 days and their moderately asymmetric profile can result from the overlapping of subsequent episodes. In a few cases, significant variations by a factor of two within 12 hr were detected. To have a better estimate of the rising and decaying timescales, we fit two rapid flares, with an almost regular shape, using an analytical law of the form $A \cdot \exp^{t/\tau}$. In the case of the flare peaking at $t \simeq 54846$ MJD (dashed black line in panel (b) of Figure 2), we find a rise faster than the decay: the rising timescale is $\tau \simeq 0.3$ days and the decaying one is $\simeq 1.4$ days. The second event (flare peaking at $t \simeq 54962$ MJD; dashed black line in panel (d) of Figure 2) followed the opposite behavior, having a best-fit rising timescale of $\simeq 0.8$ days, and a decay time of $\simeq 0.25$ days. Using a bin width of 6 hr, the shape of the flare is nearly symmetric, with rise and decay e-folding time of about $\simeq 0.12$ days. Such a fast variability can constrain the radiative region size $R_{\rm rad}$ by the well-known relation

$$R_{\rm rad} \leqslant \frac{c\Delta t\delta}{1+z}, \quad (1)$$

where c is the speed of light, $\delta = 1/(\Gamma(1-\beta\cos\theta))$ is the beaming factor depending on the bulk Lorentz factor Γ and a viewing angle $\theta \simeq 1/\Gamma$, and z is the cosmological redshift. Adopting the very fast superluminal velocity reported by Homan et al. (2002; $\beta_{\rm app} \simeq 20$, in very good agreement with the results presented in Section 4.3) from $\delta \simeq \Gamma \simeq \beta_{\rm app}$ we can estimate $R_{\rm rad} \lesssim 9 \times 10^{15}$ cm (in the case of $\tau \simeq 0.25$ days). We will compare this result with other constraints derived in Section 5.1.

2.2. Gamma-ray Spectra

We analyzed the γ-ray spectral shape of PKS 1510-089 during the whole period, the quiescent state, and the four flaring episodes using three spectral models: a PL, a log parabola (LP), $dN/dE \propto E/E_0^{-\alpha_\gamma-\beta\log(E/E_0)}$ (Landau et al. 1986; Massaro et al. 2004), and a broken power law (BPL). In the case of LP spectral law, the parameter β measures the curvature around the peak. The LP distribution has only three free parameters,

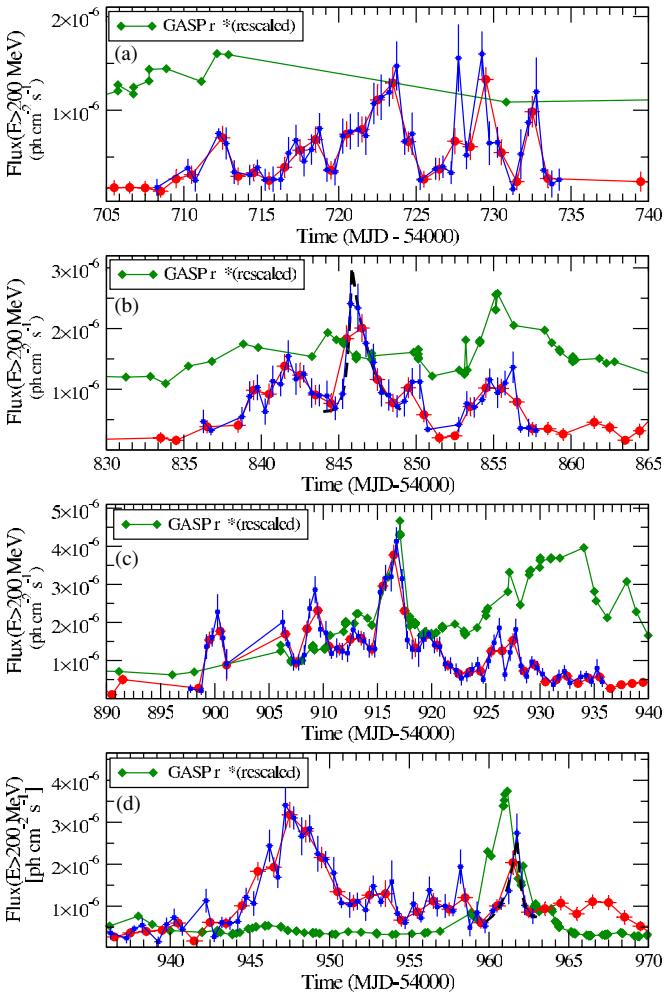

Figure 2. From top to bottom, flares a, b, c, and d showing 1 day binning (red points) and 12 hr binning (blue points). The green points represent the optical data in the *R* filter. The black dashed lines represent a best fit by means of an exponential law as described in Section 2.1.

(A color version of this figure is available in the online journal.)

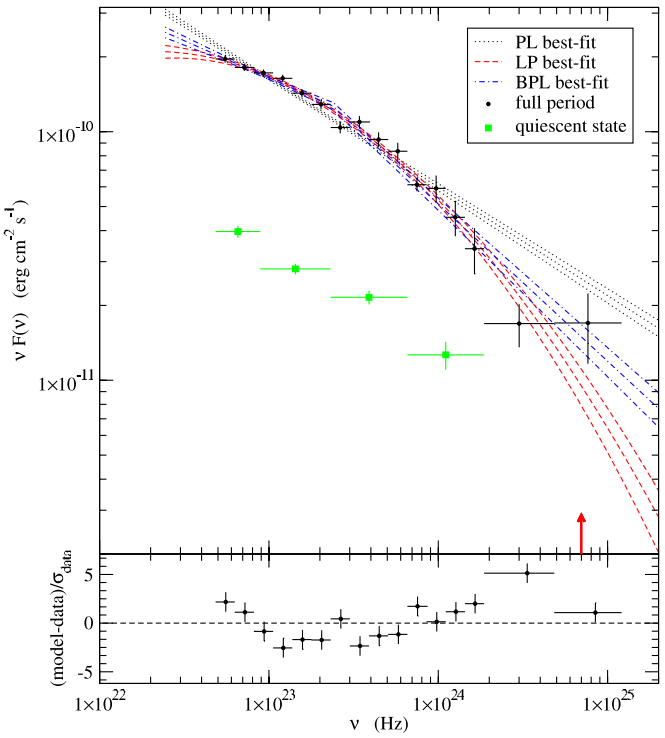

Figure 3. LAT SED of PKS 1510-089 extracted for the full period (black points) and for the quiescent state (green points). The red upward arrow indicates the highest energy event within 95% of the PSF for the whole period data set. The dotted line, the dashed line, and the dot-dashed line represent the best-fit model of the full period by means of PL, LP, and a BPL distribution, respectively, with uncertainties. The residuals in the lower panel refer to the PL model.

(A color version of this figure is available in the online journal.)

and the choice of the reference energy E_0 does not affect the spectral shape; we fixed its value to 300 MeV. We performed the spectral analysis using an unbinned maximum-likelihood estimator (`gtlike`) and the same prescription given in Section 2. We used a likelihood ratio test[84] (LRT; Mattox et al. 1996) to check the PL model (null hypothesis) against the LP model (alternative hypothesis). Since the PL is often rejected, we also test the LP model (null hypothesis) against the BPL model (alternative hypothesis). The results concerning the LRT are summarized in Table 2, and in Table 3 we report the details of the spectral analysis for each time range and spectral model. Due to the nonderivable character of the BPL law, we used also the loglikelihood profile method to determine the best-fit parameter for this model. The corresponding statistical uncertainty was estimated from the difference in the likelihood value with respect to its minimum such that $-2\Delta L = 1$. The γ-ray spectrum of PKS 1510-089 is well described by an LP, with the only exception being the quiescent state. The value of the LRT reported in Table 2 shows that both for the flares (a, b, c, d) and for the full period, the LP model describes the spectrum better than PL with a probability higher than $\simeq 99.6\%$. The BPL, in contrast, does not provide an improvement with respect to the LP model. The only exception is the flare b, but the false positive probability is about 27.33%, so there is no evidence to reject the null hypothesis. The LP model is then preferred because of the lower number of parameters. Moreover the curvature parameter β can be linked to physical processes such as the acceleration or the effects of the Klein–Nishina (KN) regime in the IC process, as we will discuss in Sections 5.1 and 5.2. For a better visualization of the SED shape and to show the departure from a PL trend, we produced an SED by performing an independent likelihood analysis starting form a grid of 20 energy bins logarithmically equispaced. The bins were then grouped in order to have at least 10 photons per bin, and the highest energy bin was chosen according to the maximum energy encircled within 95% of the point-spread function (PSF). The results are shown in Figures 3 and 4. In Figure 3, we show the full-period SED and the one extracted during the quiescent state. We plot by a dotted line the PL model, by a dashed line the LP model, and by a dot-dashed line the BPL model. With a red upward arrow, we indicate the highest energy event within 95% of the PSF for the whole period data set, corresponding to an energy of approximately 30 GeV. From the plot of the PL model residuals (lower panel), it is possible to clearly see the departure from a PL trend: the deviations, both at low and high energies, suggest for a spectral curvature confirming the LRT results. Moreover, it is possible to note that the BPL model does not deviate significantly from the LP trend, supporting again the LRT analysis. The SEDs of individual flares are plotted in Figure 4 and show that the spectrum was curved also during the single flaring episodes.

[84] The LRT statistic is defined as LRT $= -2\log(L0/L1)$, where $L0$ and $L1$ are the maximum likelihood estimated for the null and alternative hypothesis, respectively.

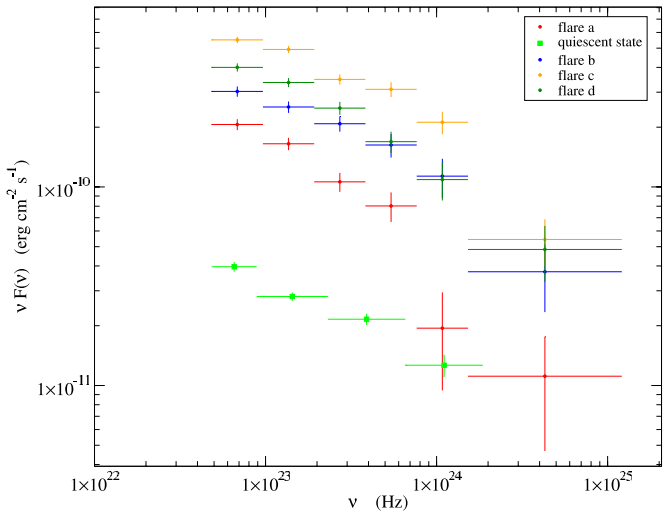

Figure 4. LAT SED of PKS 1510-089 extracted for the flaring states and for the quiescent state (green points).

(A color version of this figure is available in the online journal.)

We note that the flare-integrated spectral shape did not change significantly, despite the huge flux variations.

2.2.1. Spectral Evolution

To complete the analysis of the spectral behavior of PKS 1510-089, we investigate whether spectral changes are seen between the quiescent and the flaring state. Since we are mainly interested in the search of possible trends rather than in the best description of the spectral distribution, we simply evaluated the PL spectral indices in the various brightness states, which can be considered representative of the mean slope. In the upper panel of Figure 5, we plot the photon index against the flux above 0.2 GeV, resulting from the same spectral analysis showed in Figure 1. In the case of daily integration (green circles), and more marginally for the weekly integration (red circles), this plot seems to show a softer when brighter trend, up to a flux level of $F(E > 0.2\,\mathrm{GeV}) \simeq 2.4 \times 10^{-7}$ photons cm^{-2} s^{-1}. Above this value of the flux, the source has a harder when brighter trend. We analyze the correlation of the harder when brighter trend, for the weekly binning, using a Monte Carlo method that takes into account the dispersion of flux and index measurements. In detail, we re-sample the flux and index values for each observed pair, extracting the data from a normal distribution centered on the observed value and with a standard deviation equal to the 1σ error estimate. We find a correlation coefficient of $r = 0.43$ with a 95% confidence limit $0.24 \leqslant r \leqslant 0.58$. The trend for $F(E > 0.2\,\mathrm{GeV}) \gtrsim 2.4 \times 10^{-7}$ photons cm^{-2} s^{-1} is reported in the inset of the upper panel of Figure 5.

Although for some EGRET blazars, Nandikotkur et al. (2007) observed a similar flux-hardness anticorrelation at low fluxes, we need to take into account possible effects coming from the poor statistics when the source flux is low. As first, we note that moving to the weekly binning the trend is less evident, although the flux range is the same as that of the daily binning. As a further check, in the lower panel of Figure 5 we plot the photon index against the number of photons predicted by the best-fit model. It is clear that the dispersion of the photon index is related closely to the number of predicted photons, above $N \simeq 20$ the trend is the same for both the two integration timescales, and the photon index clusters around 2.5, without showing the very soft and very hard index values present at low number of events.

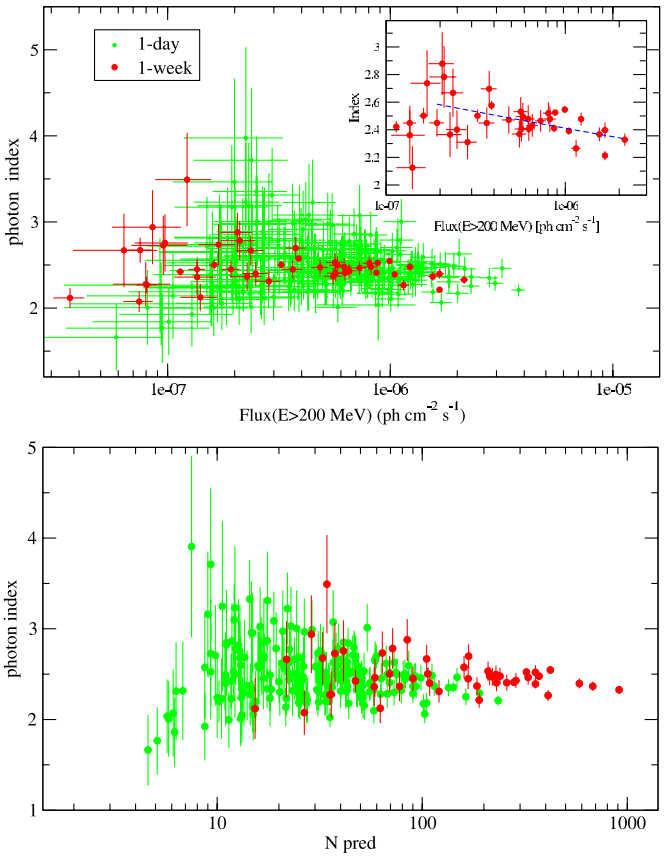

Figure 5. Upper panel: weekly and daily scatter plot of the flux ($E >$ 200 MeV) vs. the photon index (TS $>$ 10). The inset shows the same for flux ($E >$ 200 MeV) $> 2 \times 10^{-7}$ photons cm^{-2} s^{-1}. Lower panel: scatter plot of the number of photons predicted by the best-fit model vs. the photon index, for weekly and daily integration (TS $>$10).

(A color version of this figure is available in the online journal.)

In conclusion, we cannot exclude the presence of a softer when brighter trend, for low flux levels and short timescales, but the statistical effects we present do not allow to obtain a purely physical interpretation. Similar results have been found for other *Fermi* Blazars (Abdo et al. 2010c), independently of their redshift or class (BL Lacs/FSRQs).

Even if we did not find a strong evidence for a index–flux correlation, the variation of the photon index returned by the `gtlike` fit as a function of time (see upper panel of Figure 1), shows that the dispersion on the photon index is larger until mid-March roughly, and gets narrower after. This feature is emphasized in Figure 6, where in the upper panel we plot the histogram of the photon index for the weekly integration, before MJD 54905 (corresponding to 2009 March 15, blue shaded histogram), and after MJD 54905 (red empty histogram). In the lower panel, we plot the same analysis for the case of daily integration. The distributions before and after MJD 54905 have the same mean, in both daily and weekly integrations ($\simeq$ 2.5), but very different standard deviations. In the case of daily integration, we have 0.45 and 0.21 before and after MJD 54905, respectively. In the case of the weekly integration, we have a standard deviation of 0.28 before MJD 54905 and 0.07 after. To test more quantitatively whether or not the distributions are different, we use a Kolmogorov–Smirnov (KS) test. We applied the test to the distributions of the spectral indices before and after MJD 54905, for the daily and weekly integrations. The test returns a p-value of $\simeq$ 0.13 and $\simeq$ 0.35, for the case of

Table 2
Unbinned Likelihood LRT Summary

Time Range	−loglike(PL)	−loglike(LP)	−loglike(BPL)	LRT(PL/LP)/P.(LP)[a]	LRT(LP/BPL)/P.(BPL)[a]
Full	323082.6	323056.4	323062.8 323059.0[b]	56.2/>99.99%	−12.8/NULL −5.2/NULL
Quiescent	83057.7	83057.5	83057.6	0.4/47.3%	−0.2/NULL
Flare a	28908.9	28902.4	28903.5 28902.5[b]	6.5/99.97%	−2.2/NULL −2.0/NULL
Flare b	23932.7	23928.5	23927.9 23927.9[b]	8.4/99.62%	1.2/72.67% 1.2/72.67%
Flare c	38328.9	38318.5	38320.2 39319.4[b]	20.8/99.99%	−3.4/NULL −1.8/NULL
Flare d	31326.1	31322.0	31323.3 31322.8[b]	8.2/99.58%	−2.6/NULL −1.6/NULL

Notes.
[a] P.(LP) and P.(BPL) are the cumulative distribution functions of the LRT statistics, evaluated at the LRT value actually observed. These probabilities are evaluated using as reference distribution a χ^2_d distribution with the number of degrees of freedom (d) equal to the difference in the number of free parameters in the two models.
[b] BPL fit by means of loglikelihood profile.

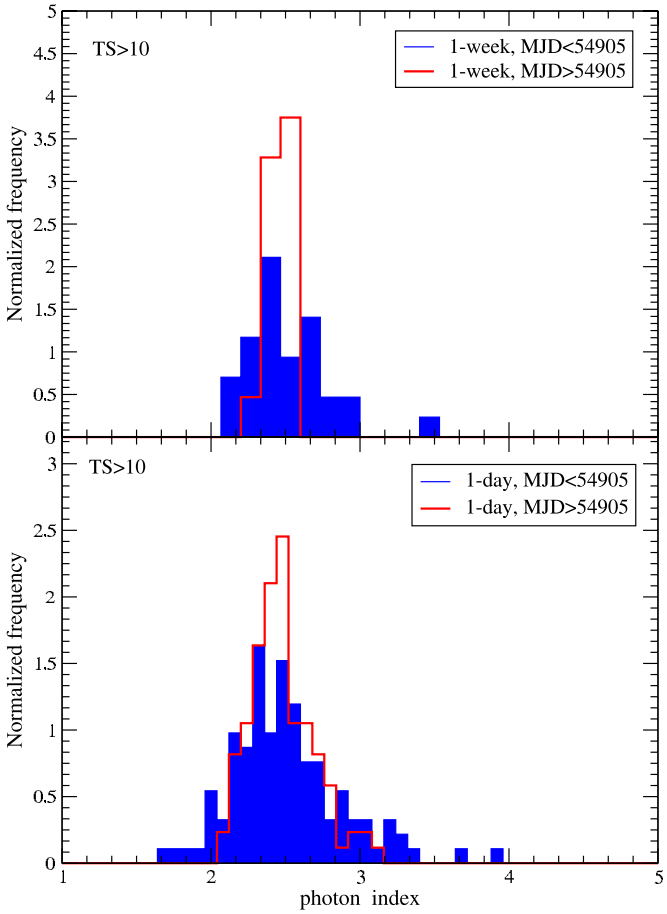

Figure 6. Upper panel: the histogram of the photon index for, a weekly integration time, before (blue) and after (red) MJD 54905, respectively. Lower panel: the same as in the upper panel, in the case of daily integration.
(A color version of this figure is available in the online journal.)

weekly and daily binning, respectively. The KS test gives only a marginal indication that the data sets, before and after MJD 54905, may not be drawn from the same distribution.

In conclusion, the typical γ-ray photon index of PKS 1510-089 is around 2.5 and values largely different from this were never observed in high states. LP best fits indicate a significant but quite mild spectral curvature, that in the brightest flares (b, c, and d) was always very close to $\beta = 0.1$.

3. MULTIFREQUENCY OBSERVATIONS AND DATA REDUCTION

The unique, high-quality data provided by the LAT instrument cannot be physically fully understood without simultaneous multifrequency observations. The spectral curvature and the spectral evolution observed in the γ-ray band, need to be compared to SED evolution from the radio to the hard X-ray. Radio data, and in particular very long baseline interferometry (VLBI) data allow us to constrain the beaming factor and to cross-check this result with that obtained from the γ-ray transparency. X-ray data can shed light on the balance between the SSC and the ERC component, and allow us to estimate the spectral shape of the low-energy branch of the electron energy distribution. UV data provide information about the big blue bump (BBB) radiation, and combined with optical data tell us about the high-energy branch of the electron distribution. Moreover, UV/optical data constrain the peak flux and energy of the low-energy bump, determining the ratio between the output of the synchrotron distribution to that of the IC one.

In the following subsections, we report the reduction of the data collected at different wavelengths as a result of pre-planned campaigns (GLAST-*AGILE* Support Program (GASP) optical-to-radio and VLBI radio data) or as ToO triggered by the LAT flaring activity (*Swift* data). In the next section (Section 4), we discuss the MW results and their connection to the LAT data.

3.1. SWIFT-BAT and XRT Data

We analyzed XRT (Burrows et al. 2005; Gehrels et al. 2004) data using the `xrtpipeline` tool provided by the `HEADAS v6.7` software package, for data observed in photon counting mode. Events in the 0.3–10 keV energy band were extracted, selecting grades in the range 0–12, and default screening parameters to produce level 2 cleaned event files were applied. Due to the low count rate (<2 counts s^{-1}), we did not find any signature of the pile-up effect.

We used data from the Burst Alert Telescope (BAT) on board the *Swift* mission to derive the spectrum of PKS 1510-089 in the

Table 3
Unbinned Likelihood Spectral Fit Results

Time Range	PL			LP				BPL[a]				
	α_γ	F_{100}[b]	loglike	α_γ	β	F_{100}[b]	loglike	α_γ	α_{γ_1}	E_b[c]	F_{100}[b]	loglike
Full	2.44 ± 0.01	1.32 ± 0.03	323082.6	2.23 ± 0.02	0.09 ± 0.01	1.12 ± 0.03	323056.4	2.30 ± 0.02	2.63 ± 0.04	980 ± 130	1.37 ± 01	83057.6
								...	...	...	...	...
Quiescent	2.43 ± 0.07	0.27 ± 0.03	83057.7	2.3 ± 0.1	0.03 ± 0.05	0.25 ± 0.04	83057.5	2.5 ± 1.5	2.4 ± 1.5	700 ± 8000	0.3 ± 02	28903.5
								...	...	...	...	...
Flare *a*	2.55 ± 0.01	1.55 ± 0.02	28908.9	2.2 ± 0.1	0.19 ± 0.06	1.16 ± 0.12	28902.4	2.39 ± 0.01	3.22 ± 0.04	1500 ± 40	1.37 ± 0.01	28903.5
								...	...	...	...	...
Flare *b*	2.35 ± 0.04	2.1 ± 0.1	23932.7	2.0 ± 0.1	0.10 ± 0.03	1.7 ± 0.1	23928.5	2.26 ± 0.05	3. ± 0.03	3400 ± 800	1.9 ± 0.1	23927.9
								...	...	...	...	...
Flare *c*	2.37 ± 0.3	3.9 ± 0.1	38328.9	2.13 ± 0.06	0.1 ± 0.02	3.3 ± 0.2	38318.5	2.28 ± 0.04	2.9 ± 0.2	1918 ± 593	3.7 ± 0.1	38319.9
								...	...	...	...	...
Flare *d*	2.44 ± 0.04	2.9 ± 0.1	31326.1	2.24 ± 0.08	0.09 ± 0.03	2.5 ± 0.1	31322.0	2.31 ± 0.08	2.6 ± 0.1	1000 ± 300	2.6 ± 0.1	31323.3

Notes.
[a] BLP fit by means of loglikelihood profile.
[b] 10^{-6} photons cm^{-2} s^{-1}.
[c] MeV.

14–195 keV band. The spectrum is constructed by averaging the spectra of the source extracted over short exposures (e.g., 300 s) and it is representative of the sources emission over the five year time range spanned by the observations. These spectra are accurate to the mCrab level and the reader is referred to Ajello et al. (2008, 2009a, 2009b) for more details. PKS 1510-089 is bright in BAT and the approximate significance of the BAT spectrum used for this analysis is $\simeq 13\sigma$.

3.2. Swift-UVOT Data

We followed the steps outlined in the UVOT User's Guide, to perform UVOT data reduction and analyses in all the six available filters (*V*, *B*, *U*, UV*W1*, UV*M2*, and UV*W2*). We started from the raw data stored in the HEASARC archive and we made sure that the sky coordinates were updated, the modulo-8 correction was applied, duplicated FITS extensions have been removed, and the aspect correction was calculated. Based on the active galactic nucleus (AGN) intensity, the optimal source extraction region is a 5″ circle. The background region is an annulus with inner–outer radii of 15″–27″, 27″–35″, depending on the filter used. In order to improve the astrometry, the NASA/IPAC Extragalactic Database (NED) position has been adjusted using the uvotcentroid task, and field of view sources have been excluded from the background region. The standard output of the uvotsource task has been used to extract the photometric light curves. We corrected the magnitudes for Galactic extinction assuming $E(B-V)_{\rm Gal} = 0.097$ mag. This value was calculated from Schlegel et al. (1998) tables using tools provided by the NASA/IPAC archive.[85] The absorption for the other filters was calculated according to the extinction laws of Cardelli et al. (1989). The de-reddened magnitudes were converted into fluxes in physical units taking into account the zero points by Poole et al. (2008).

3.3. Optical Near-IR and Radio Observations by GASP

GASP is performing a long-term monitoring of 28 γ-ray loud blazars in the optical, near-infrared, millimeter, and radio bands (Villata et al. 2008, 2009b). The GASP has been following PKS 1510-089 since 2007 January, and contributed to MW studies involving γ-ray data from *AGILE* (Pucella et al. 2008; D'Ammando et al. 2009a). The optical and near-infrared GASP data for the present paper were acquired at the following observatories: Abastumani, Armenzano, Calar Alto, Campo Imperatore, Castelgrande, Crimean, Kitt Peak (MDM), L'Ampolla, Lowell (Perkins), Lulin, Roque de los Muchachos (KVA and Liverpool), Sabadell, San Pedro Martir, St. Petersburg, Talmassons, and Valle d'Aosta. Magnitude calibration was performed with respect to a common choice of reference stars in the field of the source from the photometric sequence by Raiteri et al. (1998). Conversion of magnitudes into de-reddened flux densities was obtained by adopting the Galactic absorption value $A_B = 0.416$ from Schlegel et al. (1998), consistent with the $E(B-V)$ color excess, the extinction laws by Cardelli et al. (1989), and the mag-flux calibrations by Bessell et al. (1998).

The GASP millimeter-radio data were taken at Medicina (5, 8, and 22 GHz), Metsähovi (37 GHz), Noto (43 GHz), SMA (230 GHz), and UMRAO (4.8, 8.0, and 14.5 GHz).

[85] The NASA/IPAC Extragalactic Database (NED) is operated by the Jet Propulsion Laboratory, California Institute of Technology, under contract with the National Aeronautics and Space Administration.

3.4. VLBI Data

The 2 cm VLBA/MOJAVE program (Lister et al. 2009b and references therein) has been monitoring PKS 1510-089 at 15 GHz with the Very Long Baseline Array (VLBA) since 1995. Method of observations, data processing, and imaging is discussed by Lister et al. (2009b). Typical resolution of these images is about or better than 3 pc.

In addition to the 15 GHz MOJAVE VLBA monitoring, single-epoch simultaneous multifrequency 5–43 GHz VLBA measurements were done on 2009 April 9, in support of the first year *Fermi* observations (Sokolovsky et al. 2010). Accuracy of flux density measurements is dominated by calibration uncertainties: about or less than 5% at 5, 8, and 15 GHz, about our less than 10% at 24 and 43 GHz.

4. MULTIFREQUENCY RESULTS AND CONNECTION WITH THE LAT DATA

4.1. X-ray and Hard-X-ray Data

We performed the spectral analysis of *Swift*-XRT data after grouping the photons to have a minimum number of 10 photons per bin, and we fitted the spectra by means of a *photon* PL distribution $F(E) = KE^{-\alpha_X}$, plus a Galactic absorption with an equivalent column density $N_H = 7.88 \times 10^{20}$ cm^{-2} (Lockman & Savage 1995). We extracted the X-ray spectrum for each pointing. The corresponding spectral analysis results are reported in Table 4.

The X-ray light curve obtained from the fluxes reported in Table 4 shows a modest variability if compared to optical and γ-ray flares (see Figure 7). We prefer to present light curves in terms of $\nu F(\nu)$ to make easier the comparison between the various bands and the SED changes. The average flux integrated in the 0.3–10.0 keV range is around 10^{-11} erg cm^{-2} s^{-1}, the lowest flux, recorded on 2009 January 16, was $(6.5 \pm 0.8) \times 10^{-12}$ erg cm^{-2} s^{-1}. The highest flux, recorded on 2009 April 28, was $(15.0 \pm 1.5) \times 10^{-12}$ erg cm^{-2} s^{-1}. In this case, the flux increased by a factor of 2 within a day, and the spectrum reached the hardest state ($\alpha_X = 1.13 \pm 0.13$). This is the most relevant X-ray flaring episode in our data set and looking at the MW light curve in Figure 7 it seems to have no counterparts in other wavelengths. Since the statistics are low, we performed the spectral analysis using the Cash method (C-stat; Cash 1979) based on the use of a likelihood function. This method returns flux and photon index values that are compatible with those coming from the χ^2 method. Even if the two methods results are compatible, the significance of this flare is low ($\simeq 2\sigma$), so we do not investigate possible physical implications.

During our observations, the source spectrum was always hard, with a photon index ranging between about 1.3 and 1.6. The plot of the flux in 0.3–10.0 keV range versus the photon index (see Figure 8) is compatible with a harder when brighter trend. Using the Monte Carlo method described in Section 2.2.1, we get a correlation coefficient $r = -0.31$ with a 95% confidence limit of $-0.55 \leqslant r \leqslant -0.05$. This spectral trend is consistent with the same analysis performed by Kataoka et al. (2008). We note also that Kataoka et al. (2008) found a soft-X-ray excess in the *Suzaku* data, but the statistics of the individual pointings in our data set are not sufficient to detect such a feature.

In order to increase the statistics and to look for differences between the different γ-ray flares, we produced X-ray SEDs averaged during the b, c, and d γ-ray flaring intervals, and during

Table 4
Spectral Analysis of XRT Data

Observation Date	Start Time MJD (days)	Norm (10^{-4})	α_X	Flux 0.3–10 keV (10^{-12} erg cm^{-2} s^{-1})	χ_r^2/dof
2009 Jan 10	54841.8	$9.4^{+0.6}_{-0.6}$	$1.35^{+0.07}_{-0.08}$	$8.5^{+0.8}_{-0.6}$	0.697(43)
2009 Jan 11	54842.9	$9.4^{+0.6}_{-0.6}$	$1.28^{+0.07}_{-0.07}$	$9.4^{+0.7}_{-0.7}$	0.817(46)
2009 Jan 13	54844.0	$9.9^{+0.7}_{-0.7}$	$1.46^{+0.08}_{-0.08}$	$7.9^{+0.6}_{-0.6}$	0.978(38)
2009 Jan 14	54845.8	$10.4^{+0.7}_{-0.6}$	$1.41^{+0.07}_{-0.07}$	$8.8^{+0.7}_{-0.9}$	0.811(46)
2009 Jan 16	54847.7	$10.2^{+0.7}_{-0.7}$	$1.45^{+0.07}_{-0.07}$	$8.2^{+0.8}_{-0.8}$	0.778(42)
2009 Jan 16	54849.2	$8.0^{+0.8}_{-0.8}$	$1.44^{+0.12}_{-0.12}$	$6.5^{+0.8}_{-0.8}$	0.571(20)
2009 Jan 21	54852.8	$9.8^{+0.6}_{-0.6}$	$1.41^{+0.07}_{-0.07}$	$8.3^{+0.7}_{-0.7}$	0.898(51)
2009 Jan 25	54856.8	$9.6^{+0.7}_{-0.7}$	$1.36^{+0.09}_{-0.09}$	$8.7^{+0.8}_{-0.8}$	0.832(30)
2009 Mar 6	54896.9	$8.9^{+1.2}_{-1.2}$	$1.5^{+0.2}_{-0.2}$	$7.1^{+1.2}_{-1.4}$	0.980(11)
2009 Mar 11	54901.6	$11.8^{+0.6}_{-0.6}$	$1.62^{+0.06}_{-0.06}$	$7.8^{+0.6}_{-0.5}$	1.067(68)
2009 Mar 12	54902.6	$13.1^{+0.6}_{-0.6}$	$1.58^{+0.05}_{-0.06}$	$9.1^{+0.6}_{-0.6}$	0.897(78)
2009 Mar 17	54907.2	$10.7^{+0.6}_{-0.6}$	$1.6^{+0.07}_{-0.07}$	$7.2^{+0.6}_{-0.6}$	1.184(61)
2009 Mar 18	54908.0	$9.9^{+0.5}_{-0.5}$	$1.45^{+0.06}_{-0.06}$	$8^{+0.6}_{-0.5}$	0.949(59)
2009 Mar 19	54909.8	$12.1^{+0.8}_{-0.8}$	$1.69^{+0.09}_{-0.09}$	$7.4^{+0.8}_{-0.6}$	1.049(35)
2009 Mar 20	54910.9	8.7^{+1}_{-1}	$1.3^{+0.14}_{-0.14}$	$8.5^{+1.2}_{-1.2}$	1.210(20)
2009 Mar 22	54912.1	$9.9^{+0.9}_{-0.8}$	$1.46^{+0.11}_{-0.11}$	$7.9^{+0.8}_{-0.8}$	1.325(30)
2009 Mar 22	54912.1	$16.5^{+1.4}_{-1.4}$	$1.69^{+0.1}_{-0.1}$	$10.1^{+1.2}_{-1.2}$	0.506(20)
2009 Mar 23	54913.5	$9.3^{+0.7}_{-0.7}$	$1.47^{+0.1}_{-0.1}$	$7.3^{+0.6}_{-0.7}$	0.983(30)
2009 Mar 24	54914.1	$10.2^{+0.9}_{-0.9}$	$1.56^{+0.12}_{-0.11}$	$7.3^{+0.8}_{-0.7}$	0.770(23)
2009 Mar 25	54915.6	$11.1^{+0.8}_{-0.8}$	$1.51^{+0.08}_{-0.08}$	$8.4^{+0.9}_{-1}$	1.293(37)
2009 Mar 26	54916.7	10.6^{+1}_{-1}	$1.54^{+0.12}_{-0.12}$	$7.6^{+1.1}_{-1.3}$	1.084(19)
2009 Mar 27	54917.2	9.9^{+1}_{-1}	$1.53^{+0.12}_{-0.12}$	$7.3^{+1.1}_{-0.8}$	0.840(19)
2009 Mar 28	54918.2	$10.0^{+0.7}_{-0.7}$	$1.35^{+0.08}_{-0.08}$	$9.1^{+0.9}_{-0.7}$	0.777(32)
2009 Mar 30	54920.4	$11.8^{+0.9}_{-0.9}$	$1.41^{+0.08}_{-0.08}$	10^{+1}_{-1}	0.855(31)
2009 Apr 4	54925.5	$8.1^{+1.3}_{-1.4}$	$1.2^{+0.2}_{-0.2}$	8^{+1}_{-2}	1.775(12)
2009 Apr 10	54931.0	$10.5^{+0.7}_{-0.6}$	$1.5^{+0.07}_{-0.07}$	$8^{+0.6}_{-0.7}$	1.098(46)
2009 Apr 27	54948.6	$12.7^{+1.3}_{-1.3}$	$1.62^{+0.13}_{-0.13}$	$8.4^{+1}_{-1.3}$	0.502(15)
2009 Apr 28	54949.6	12.0^{+2}_{-2}	$1.13^{+0.13}_{-0.13}$	15^{+3}_{-2}	0.446(13)
2009 Apr 29	54950.8	$11.7^{+1.1}_{-1}$	$1.36^{+0.11}_{-0.11}$	$10.5^{+1.2}_{-1.1}$	0.951(25)
2009 May 1	54952.6	10.0^{+2}_{-2}	$1.5^{+0.2}_{-0.2}$	$7.7^{+1.7}_{-1.2}$	1.327(08)
2009 May 2	54953.4	13.0^{+1}_{-1}	$1.58^{+0.1}_{-0.1}$	$9^{+1.2}_{-0.8}$	1.241(29)
2009 May 3	54954.8	$11.9^{+1.5}_{-1.5}$	$1.5^{+0.2}_{-0.2}$	9^{+2}_{-2}	0.838(10)
2009 May 4	54955.7	10.0^{+2}_{-2}	$1.2^{+0.2}_{-0.2}$	11^{+2}_{-3}	1.428(08)
2009 May 5	54956.7	$10.5^{+0.9}_{-0.9}$	$1.53^{+0.11}_{-0.12}$	$7.7^{+0.7}_{-0.8}$	0.838(22)
2009 May 7	54958.4	$10.1^{+0.8}_{-0.8}$	$1.28^{+0.08}_{-0.08}$	$10.1^{+0.9}_{-1}$	1.122(30)
2009 May 11	54962.5	$5.4^{+1.4}_{-1.5}$	$0.9^{+0.3}_{-0.3}$	10^{+3}_{-2}	1.660(05)
2009 May 12	54963.3	$13.6^{+0.7}_{-0.7}$	$1.43^{+0.06}_{-0.06}$	$11.2^{+0.8}_{-0.8}$	0.931(62)
2009 May 13	54964.1	$12.3^{+0.6}_{-0.6}$	$1.6^{+0.06}_{-0.06}$	$8.3^{+0.5}_{-0.6}$	0.822(59)
2009 May 14	54965.3	$11.1^{+0.6}_{-0.6}$	$1.48^{+0.06}_{-0.06}$	$8.6^{+0.6}_{-0.8}$	1.175(56)
2009 May 30	54981.4	12.0^{+4}_{-4}	$1.7^{+0.4}_{-0.5}$	7^{+3}_{-2}	0.768(02)
2009 Jun 7	54989.7	17.0^{+2}_{-2}	$1.8^{+0.2}_{-0.2}$	$9.2^{+1.2}_{-1.4}$	1.575(16)
2009 Jun 13	54995.6	$11.6^{+1.3}_{-1.3}$	$1.35^{+0.14}_{-0.14}$	$10.6^{+1.5}_{-1.2}$	1.185(20)
2009 Jun 20	55002.5	$16.0^{+1.2}_{-1.2}$	$1.86^{+0.1}_{-0.1}$	$8.3^{+0.8}_{-0.8}$	0.888(24)

Note. In the last column, we report the reduced χ^2 and in parentheses, the degree of freedom.

the post-d flaring period, reported in Figure 9. These SEDs show that the average state of the X-ray emission was almost steady, without drastic differences between the flares and the post-flare integration period. We also note that a possible soft-X-ray excess is visible in the post-b flare-averaged SED. The scatter plot in Figure 10 shows no correlation between the XRT flux and the LAT flux. This absence of correlation is relevant to the understanding of the emission scenario that we will discuss in Section 5.

The five year integrated BAT SED is plotted in Figure 9. The photon index, in the 14–150 keV band, is $1.37^{+0.08}_{-0.19}$. Despite the long integration time of the BAT data, the photon index value is almost compatible with the range of values observed in the XRT data in our data set, and in other historical observations. This suggests that the X-ray and hardX-ray flux and spectral shape of this source are quite stable, or at least that our X-ray sampling is representative of the X-ray and hard X-ray shape on timescales of years.

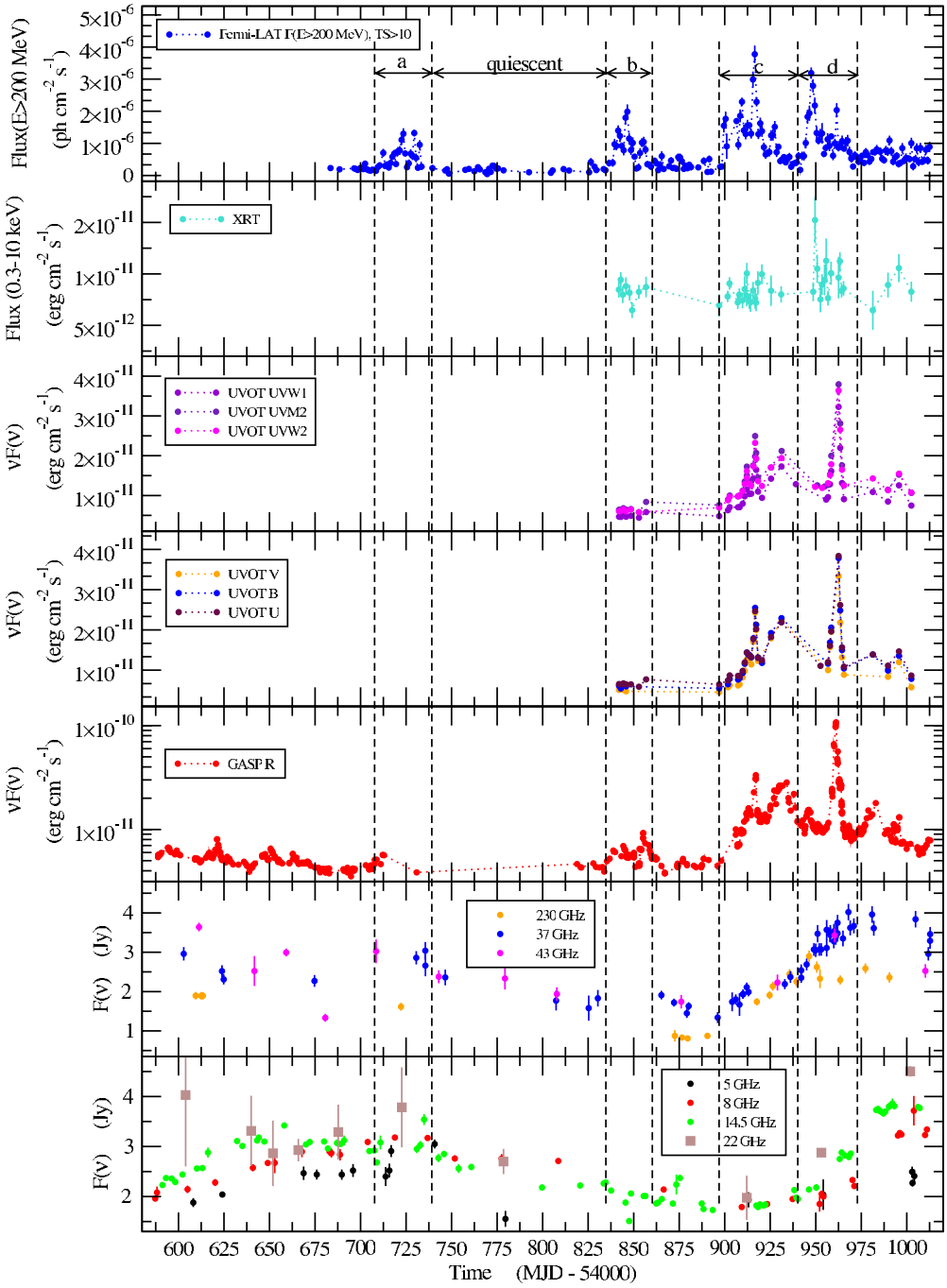

Figure 7. MW light curves, from 2008 April to 2009 June. The vertical dashed lines show the four flaring episodes and the quiescent state.
(A color version of this figure is available in the online journal.)

4.2. Optical/Near-IR and UV Data Results

Simultaneous *Swift*-UVOT and GASP observations provide a valuable data set to study the low-energy bump of the SED. In Figure 11, we plot the SEDs obtained from UVOT and GASP data, simultaneous within a daily timescale. These data show a minimum around the frequency of 5×10^{14} Hz, which does not seem to vary when the source is flaring. The frequency of the high-energy peak can be estimated well and is close to 10^{15} Hz, while that of the peak at low frequency cannot be well established and should be roughly estimated around 10^{13} Hz. The UV peak, as in many quasars, is likely due to the BBB that usually is understood as thermal emission from the accretion disk surrounding the BH. Assuming that the disk luminosity is steady or slowly variable compared to the synchrotron emission, we expect that the UV excess gets less and less evident, as the optical flux increases. To test this scenario, in Figure 12 we plot the ratio of the flux in the highest energy UVOT filter (UV*W2*) to the flux in the *B* UVOT filter, as a function of the optical *R* flux. This plot shows that the UV spectrum gets harder when the optical *R* flux is lower. This trend is consistent with the UV excess decreasing as the *R* flux is increasing, as expected in a scenario in which the UV bump originates in the thermal emission of the accretion disk. Despite this trend, we note that even in the highest state plotted in Figure 11, the corresponding UV bump is still prominent. For other FSRQs, such as 3C 454.3,

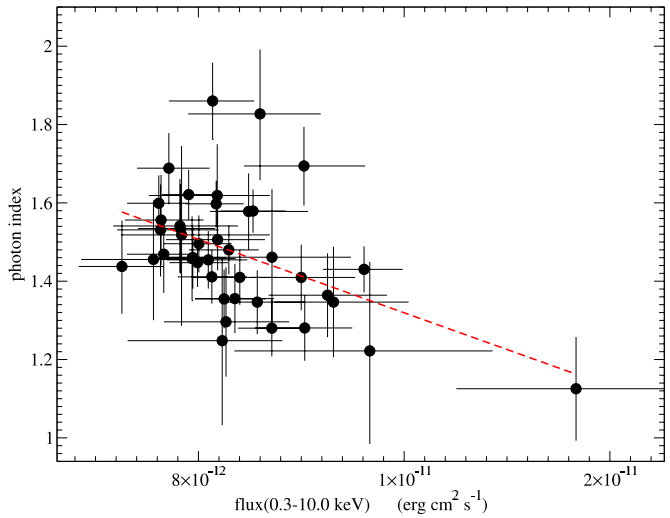

Figure 8. Scatter plot of the flux in 0.3–10.0 keV range vs. the X-ray photon index (α_X). The dashed lines represent a linear bet fit model. Using the Monte Carlo method described in Section 2.2.1, we get a correlation coefficient $r = -0.31$ with a 95% confidence limit of $-0.55 \leqslant r \leqslant -0.05$.

(A color version of this figure is available in the online journal.)

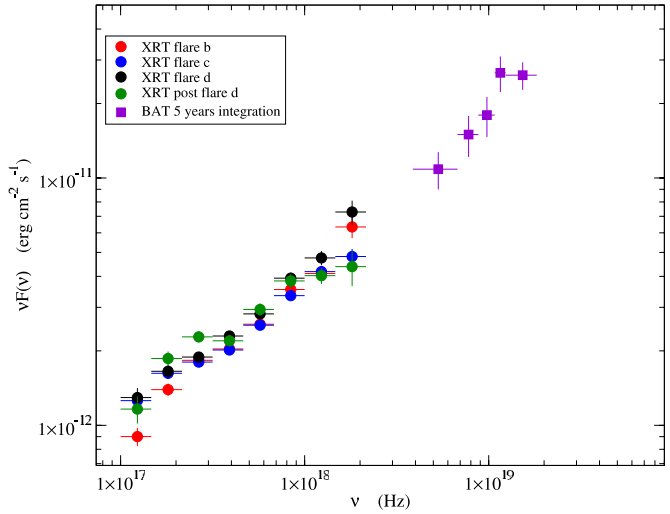

Figure 9. XRT SEDs averaged during the flares b, c, and d and during the post-d flare period. The violet boxes represent the BAT spectrum averaged over five years.

(A color version of this figure is available in the online journal.)

the BBB is not visible during the high optical states (Giommi et al. 2006; Villata et al. 2006), since it is dominated by the synchrotron flux, as we would expect here in the case of PKS 1510-089. In panels (a) and (b) of Figure 13 UV light curves for all the six filters are shown, and in panel (c) we plot the ratio of the UVOT *V* filter flux to the UVOT *W2* filter. The trend of the hardness ratio is clearly anticorrelated with that of the fluxes. Again, this supports the BBB scenario, with the UV spectrum harder when the BBB is more evident, namely, when the synchrotron flux is lower.

In Figure 14, we report the scatter plot of the *Fermi*-LAT flux $F(E > 200$ MeV) versus the UVOT νF(ν) in the UV*W2* filter, to check for a possible significant correlation between the γ-ray and UV fluxes. The correlation coefficient of the logarithms of the UV and γ-ray fluxes, obtained through the Monte Carlo method described in Section 2.2.1, is $r = 0.2$ with a 95% confidence interval of $0.05 \leqslant r \leqslant 0.34$. If we

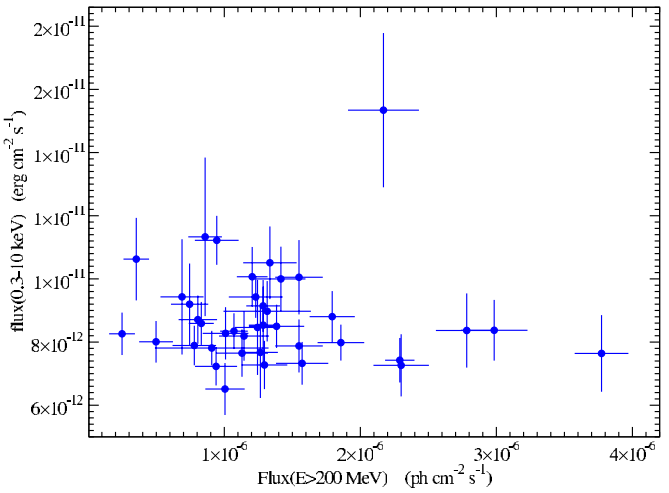

Figure 10. Scatter plot of the XRT flux in the 0.3–10 keV band vs. the *Fermi*-LAT flux ($E > 200$ MeV).

(A color version of this figure is available in the online journal.)

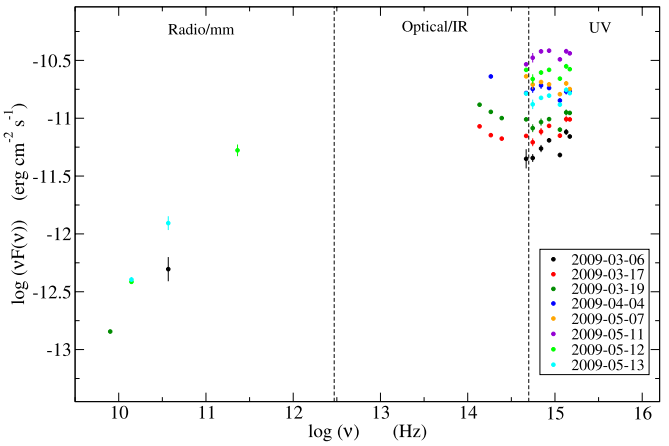

Figure 11. Radio to UV SEDs built using only data simultaneous within a daily time span.

(A color version of this figure is available in the online journal.)

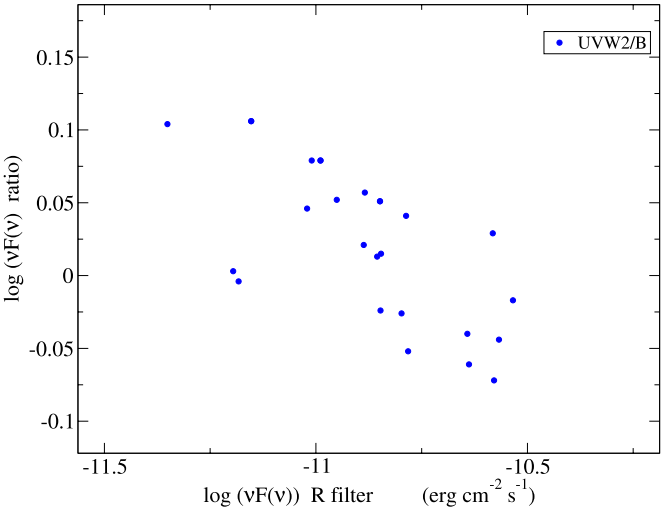

Figure 12. Ratio of $\nu F(\nu)$ in the UVOT UV*W2* filter to $\nu F(\nu)$ in the UVOT *B* filter, as a function of $\nu F(\nu)$ in the optical *R* filter.

(A color version of this figure is available in the online journal.)

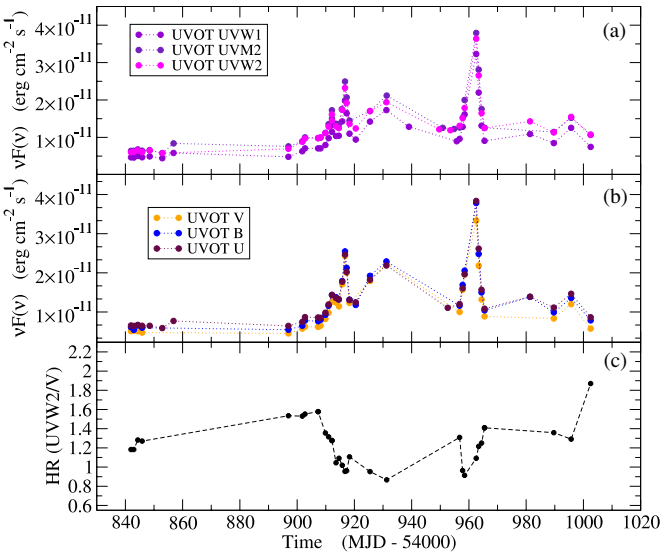

Figure 13. Panels (a) and (b): UVOT light curves. Panel (c): hardness ratio of the UVOT spectra (UV*W2*/UV*V*) evaluated as a function of the time.

(A color version of this figure is available in the online journal.)

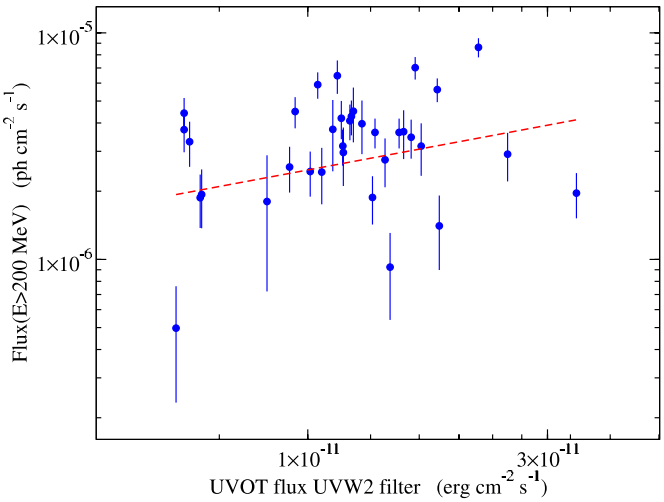

Figure 14. Scatter plot of the *Fermi*-LAT flux ($E > 200$ MeV) vs. the UVOT $\nu F(\nu)$ in the UV*W2* filter. The red dashed line represents the best-fit power-law model. The correlation coefficient of the logarithm of the UV and γ-ray fluxes is $r = 0.2$ with a 95% confidence interval of $0.05 \leqslant r \leqslant 0.34$.

(A color version of this figure is available in the online journal.)

exclude the point with the lowest γ-ray flux, the correlation coefficient is $r = 0.05$, suggesting that the overall correlation is not significant.

This lack of correlation hints that the spectral evolution of the UV spectrum results from the contamination of the high-energy branch of the synchrotron emission, and that a change in the BBB luminosity is not the driver of the γ-ray luminosity variations. We will discuss this in Section 5.

The optical (*R* band) and near-IR (*J, H*, and *K* bands) observations span the period from 2008 May until the end of 2009 June. In Figure 15, we report the light curves of the optical data. The best sampled band is the *R* one, with more than 600 observations. The optical flaring activity increased dramatically after mid-2009 March, corresponding to the γ-ray flare c. On 2009 May 8, the source was very bright with an *R* magnitude of 13.60 ± 0.02 (Larionov et al. 2009a), and in 2 days it reached its historical peak at $R = 13.07 \pm 0.02$, about 1.3 mag brighter than the previous record level, observed on March 27 (Larionov et al. 2009b) of the same year. This dense monitoring is fundamental to understand the correlation between the optical and the γ-ray activity, both for the long-term trends and the single flares. In Figure 16, we show the scatter plot of the *Fermi*-LAT flux $F(E > 200$ MeV) versus the optical $\nu F(\nu)$ in the *R* filter. The correlation coefficient of the logarithm of the optical and γ-ray fluxes, evaluated through the Monte Carlo method described in Section 2.2.1, is $r = 0.42$ with a 95% confidence interval $0.36 \leqslant r \leqslant 0.46$, higher than that found for the UV band. This finding hints that the driver of the flaring activity can be a change in the high-energy branch of the electron distribution. We will investigate this scenario more accurately in Section 5. Despite the statistical significance of this result, there is an evident dispersion in the scatter plot that could be related to the inter-band time lags. Indeed, temporal lags could be related to the internal source photon absorption, to the cooling time of the radiating particles, or to inhomogeneities in the emitting region. To search for possible time lag between the optical (*R* band) and the γ-ray band, we used the discrete cross-correlation function (DCCF) method. Taking into account the whole data set, the DCCF analysis returns a lag of 13 ± 1 days, with the γ-ray band leading the optical one (see Figure 17, top panels). Since the *R* flux increased dramatically after the end of 2009 February, we divide the data set in two sections, before and after MJD 54890 (corresponding to 2009 Feburary 28). The DCCF results, plotted in the middle panels of Figure 17, show that the 13 day delay is still apparent. The same result holds if we analyze individually the flaring sequences d and b (Figure 17, bottom panels). Looking at the flare light curves, it is clear that the 13 day lag is caused by a change in the relative flux of the two bands such that the γ-ray flux is stronger in the first part of the flare and the *R*-band flux gets stronger in the second half. We plot in the lower panel of Figure 18 the LAT light curve above 200 MeV, and in the upper panel the optical light curve, backward shifted by 13 days: the four γ-ray flares a, b, c, d, seem to have an optical counterpart. In particular, the peaks of the bright events in May would be very close in time to those in the LAT daily light curve at MJD $\simeq$ 54948 (see Figure 2). To check the effect of this lag, we evaluate the correlation between the logarithms of the optical and γ-ray flux after applying the above time shift (see Figure 19) and find $r = 0.62$ with a 95% confidence interval $0.57 \leqslant r \leqslant 0.66$. The values of the correlation coefficient and of its 95% confidence interval, after applying the 13 days time shift, are significantly higher than those obtained without the time shift. Moreover, Figures 19 and 16 show that time shift reduces the dispersion in the scatter plot.

This 13 day correlation between the optical and γ-ray emission appears in the different outbursts during this flaring activity but we do not have any indication that it is a characteristic behavior related to the temporal and energetic evolution of the flares. Only through long-term simultaneous γ-ray and optical observations we may better understand the actual level of randomness of this correlation and its possible physical meaning.

4.3. Radio Results

Radio data have a much lower sampling with respect to optical and γ-ray, but at 14.5 GHz and 37 GHz it is possible to follow the overall trend of the radio flaring activity. Even if radio fluxes do not show a correlation with the optical and the *Fermi*-LAT flaring trend, it is possible to identify a large radio flare, starting at about MJD 54900 (see Figure 7). This radio flare, visible at

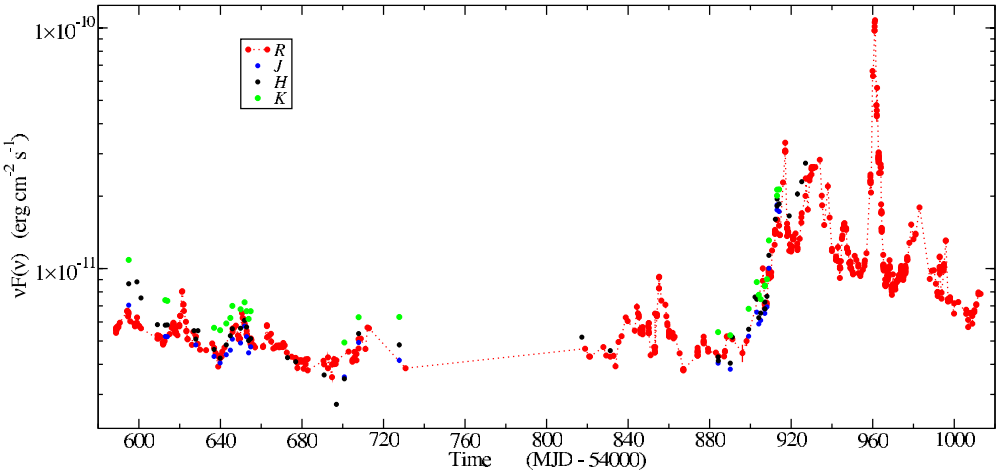

Figure 15. Optical and near-IR light curves from the GASP project.
(A color version of this figure is available in the online journal.)

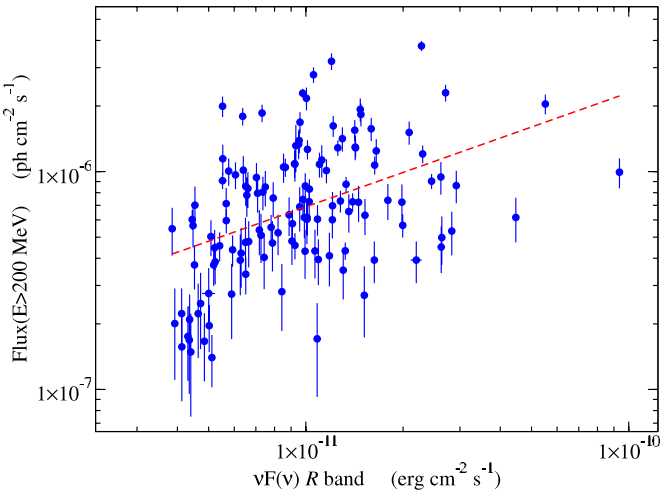

Figure 16. Scatter plot of the *Fermi*-LAT flux ($E > 200$ MeV) vs the $\nu F(\nu)$ in the optical *R* band. The dashed line represents the best-fit power-law model. The correlation coefficient of the logarithm of the optical and γ-ray fluxes, evaluated through the Monte Carlo method described in Section 2.2.1, is $r = 0.42$ with a 95% confidence interval $0.36 \leqslant r \leqslant 0.46$. There is an evident dispersion in the scatter plot, probably due to the inter-band time lags showed in Section 4.2.
(A color version of this figure is available in the online journal.)

14.5, 37, and 230 GHz, seems to start quasi-simultaneously with the γ-ray flare c at 37 GHz, and keeps increasing until the end of flare d. The 230 GHz light curve shows a structure similar to a plateau, starting when the γ-ray flare c has ended, and a possible plateau is present also at 37 GHz, starting at the end of flare d. The 14.5 GHz fluxes seem to lag behind the 37 and 230 GHz. Analysis in the radio band is much more complex than optical and γ-ray data, because of the synchrotron self-absorption and the longer cooling times, and the possibility of the overlapping of different flares.

In 2009 June and July, the integrated parsec-scale flux density had reached its historical maximum since 1995 ($\simeq 4$ Jy), as the 15 GHz MOJAVE VLBA measurements show. The VLBI core flux density has also shown the highest value (see Figure 20, upper panel). If this major radio flare, observed in the core of the parsec-scale jet, is connected to the huge γ-ray flares which have happened in the first half of 2009, this determines the source of the high-energy emission to be located around the base of the parsec-scale jet following causality arguments, as suggested by Kovalev et al. (2009). The delay between the peaks of light curves in the γ-ray and radio bands can be, at least partly, explained by the synchrotron self-absorption of the emission at radio frequencies.

In Figure 21, we present the three highest frequencies Stokes *I* parsec-scale images, from the 5–43 GHz VLBA measurements performed on 2009 April 9. The size of the bright parsec-scale core at 24 and 43 GHz is estimated to be about 60–70 μas or 0.3–0.4 pc. The core shows a flat radio spectrum (see Figure 22) indicative of a synchrotron self-absorbed region, while the first well-resolved jet feature is already optically thin radio spectral index $s_r = -0.9$ ($F(\nu) \propto \nu^{s_r}$).

The highest apparent speed of a component motion in the jet of PKS 1510-089 observed at 15 GHz by Lister et al. (2009c) is $v_{\rm app} = 24c$ which makes its jet highly relativistic and Doppler boosted, a typical case for γ-bright blazars (Lister et al. 2009a). Marscher et al. (2010a) report on two new knots, observed in VLBA images at 43 GHz. The first with an apparent speed of $24 \pm 2c$, passed the core on MJD 54674.5 $\pm$ 20 (2008 July 27). The second knot passed the core on MJD 54958.5 $\pm$ 4 (2009 May 7) which is consistent, within the estimated uncertainties, with the huge optical flare observed on 2009 May 8. A feature, coincident to the second knot, is also seen to emerge in the MOJAVE 15 GHz VLBA images from 2009 June through 2009 December. The fitted speed at 15 GHz (675 μas yr^{-1}) is somewhat slower than the Marscher et al. (2010a) speed (970 $\pm$ 60 μas yr^{-1}), but this could be due to blending with a third feature seen in the 43 GHz data to emerge sometime in 2009 June (Marscher et al. 2010b). Despite the high resolution of the 43 GHz images, a more accurate ejection date for the latter feature could not be obtained due its rapid angular evolution and close proximity (0.1 mas) to the feature ejected in 2009 May.

5. INTERPRETATION AND DISCUSSION

5.1. Physical Interpretation of γ-ray and MW Data

PKS 1510-089 was one of the brightest and most active blazars observed by *Fermi*-LAT during the first year of survey. Flaring episodes with timescales from weeks to months in addition to rapid and intense outbursts, were observed both at optical and γ-ray energies. The estimated isotropic luminosity above 100 MeV during the flare c was about 8×10^{47} erg s^{-1}. This value represents the brightest flare-averaged state of the

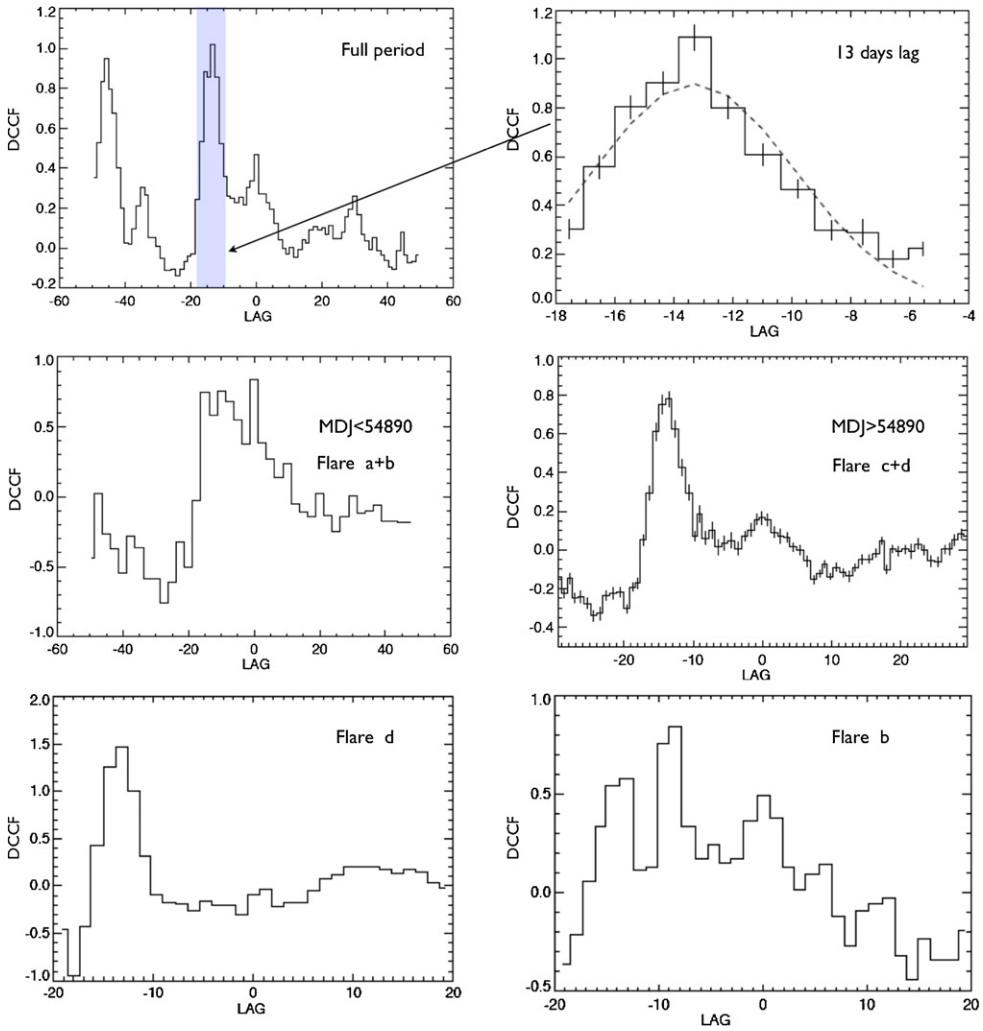

Figure 17. Top panel, left: DCCF for the whole analysis period, the shaded box concerns the 13 day lag. Top panel, right: fit by means of Gaussian distribution of the 13 day lag shaded in the left panel, the fit returns a lag of -13.4 ± 0.2, gamma leading optical. Middle panels: the DCCF for MJD $<$ 54890 (left panel) and MJD $>$ 54890 (right panel). The lag of about 13 days with the γ-ray leading the optical band is still there. Bottom panels: a lag of about 13 days (gamma leading optical) is also present for flares d and b individually.

(A color version of this figure is available in the online journal.)

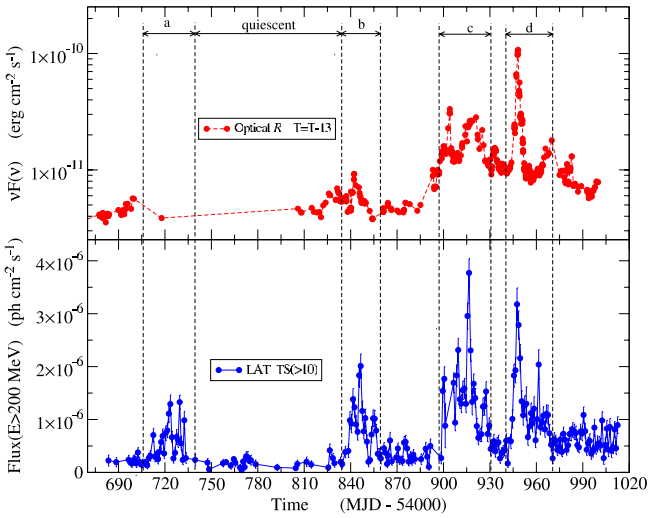

Figure 18. Upper panel: the optical (R) light curve, obtained shifting the time according to the 13 day γ-ray lag reported in Section 4.2. Lower panel: the *Fermi*-LAT light curve.

(A color version of this figure is available in the online journal.)

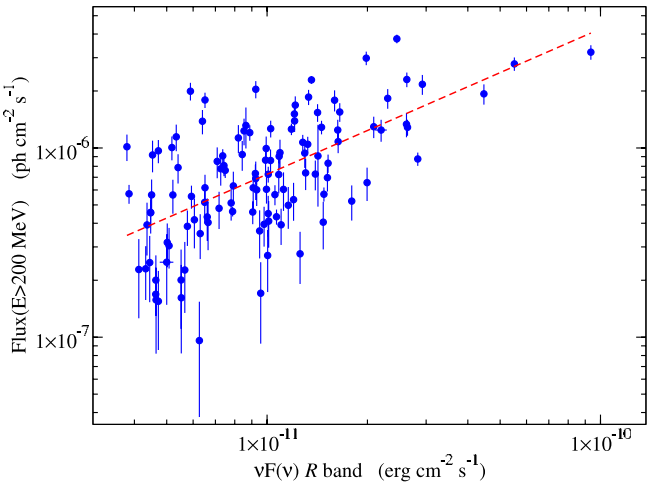

Figure 19. Scatter plot of the *Fermi*-LAT flux ($E > 200$ MeV) vs. the $\nu F(\nu)$ in the optical R band, using the time-shifted fluxes reported in Figure 18. The dashed line represents the best fit by means of a power-law model. The correlation coefficient in this case increases to $r = 0.62$ with a 95% confidence interval $0.57 \leqslant r \leqslant 0.66$.

(A color version of this figure is available in the online journal.)

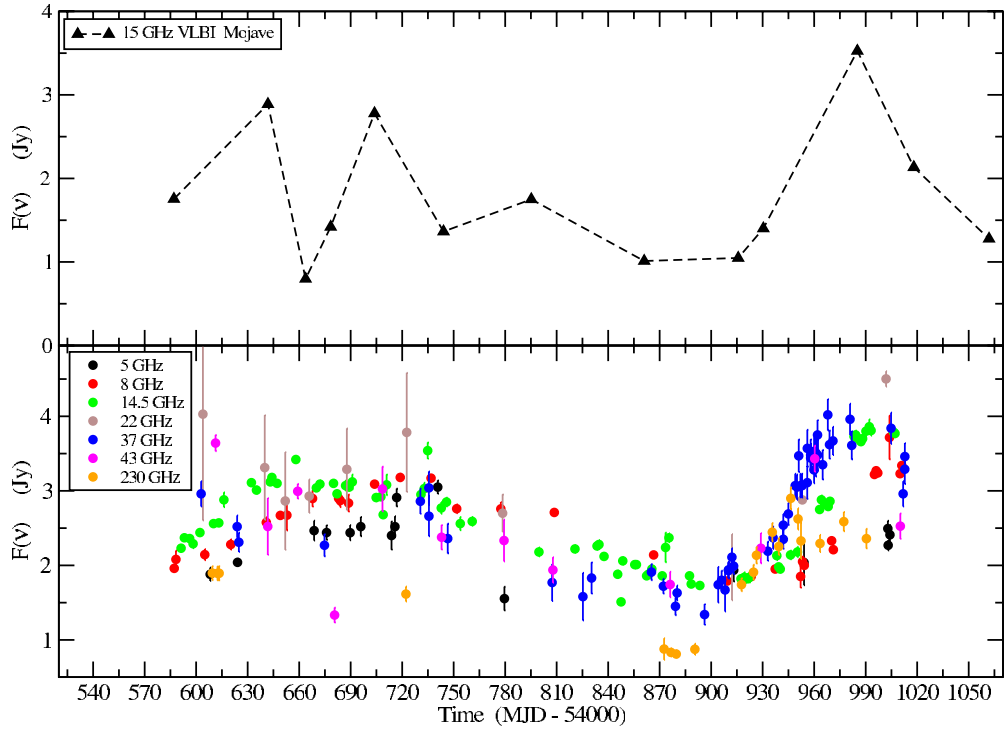

Figure 20. Upper panel: the 15 GHz MOJAVE VLBA parsec-scale core light curve. Lower panel: GASP radio light curve.
(A color version of this figure is available in the online journal.)

source. The brightest daily time-resolved luminosity, recorded during the flare c on 2009 March 26, was of $\simeq 2 \times 10^{48}$ erg s^{-1}. During the flare d, variability timescales down to a fraction of a day were observed both at optical and LAT energies.

The rapid variability and the powerful γ-ray luminosity raise the problem of the pair production opacity. Indeed, without beaming effects, the source size estimated from the observed variability timescale ($R_{\rm rad} = c\Delta t/(1+z)$) makes the source opaque to the photon–photon pair production process, provided that γ-ray and X-ray photons are produced cospatially.

If the component emerged on 2009 May 7, observed also in the MOJAVE 15 GHz VLBA, is related to the flares a and b, then we can use the value of the beaming factor derived from the motion of radio knots, namely, $\delta \simeq \Gamma \simeq \beta_{\rm app} \simeq 21$. This estimate is compatible with other VLBI estimates (Homan et al. 2002), and is slightly larger than an alternative estimate based on the variability observed at 22 and 37 GHz, $\delta_{\rm var} = 16.7$ (Hovatta et al. 2009). Taking into account the most rapid timescale estimated in Section 2.1, $\Delta t \simeq 0.25$ days, the actual emitting region size results of the order of $R_{\rm rad} \leqslant \delta \Delta t c/(1+z) \simeq 1 \times 10^{16}$ cm. Using the above fastest timescale and the quasi-simultaneous observed X-ray flux $F_X \simeq 8 \times 10^{-12}$ erg cm^{-2} s^{-1} (observed at a typical frequency of 10^{18} Hz), one can impose a limit on the minimum value of the beaming factor resulting in a source transparent to the photon–photon annihilation process (Maraschi et al. 1992; Mattox et al. 1993; Madejski et al. 1996). Combining the source size from Equation (1), the X-ray photon energy in the source frame, and the intrinsic X-ray luminosity with the optical depth expression, we get a model independent estimate of $\delta \gtrsim 8$. This lower estimate indicates that the values derived from the VLBI images are well above the pair production transparency limit.

X-ray fluxes, spectral indices, and trends in our data set are compatible with those reported in previous analysis with several X-ray telescopes (*BeppoSAX*, *ASCA*, *Suzaku*; Kataoka et al. 2008). The harder when brighter trend and the lack of X-ray/γ-ray correlation are useful to constrain both the low-energy tail of the electron distribution and the emission scenario. The typical value of the soft-to-hard-X-ray photon index α_X is close to 1.4, with a quite narrow dispersion ($\simeq 0.1$), and is similar to that observed in FSRQs with $z > 2$ (Page et al. 2005). Since in FSRQ objects the X-ray band samples the low-energy tail of the ERC component, the X-ray energy spectral index (s_X) constrains the slope p of the low-energy tail of the electron distribution in the range 1.6–2.0 ($p = 2s_X + 1$; e.g., Rybicki & Lightman 1979).

The high-energy spectral index of the electron distribution can be estimated from the optical/UV spectral shape. In Section 4.2, we showed that the optical/UV spectral index depends on the relative contamination between the synchrotron component and the BBB emission. A reliable estimate of the synchrotron spectral index could be achieved from the optical data, but, unfortunately, our spectral coverage with two or more simultaneous frequencies is only in a limited time window. In Figure 23, we plot the spectral index in the R to H bandpass versus the γ-ray flux integrated above 200 MeV. If we take into account the blue points which refer to the subflare peaking at about MJD 54909 (see Figure 2, panel (d)), we note that the γ-ray flux increased by about a factor of 2.5 with the optical spectral index almost constant around $\simeq 1$. This value of the optical spectral index corresponds to an electron energy distribution index of about 3. We note that the steadiness of the optical $R-H$ spectral index, during this γ-ray subflare, is consistent with the spectral evolution of the γ-ray emission. Indeed, extracting the γ-ray photon indices simultaneous within 1 day with the optical ones, we note that also these values are almost stable around the value of 2.4. The decay of the flare occurred with a significant spectral softening, consistent with a cooling dominated regime, with a corresponding electron spectral index in the range between 3.5 and 4.0.

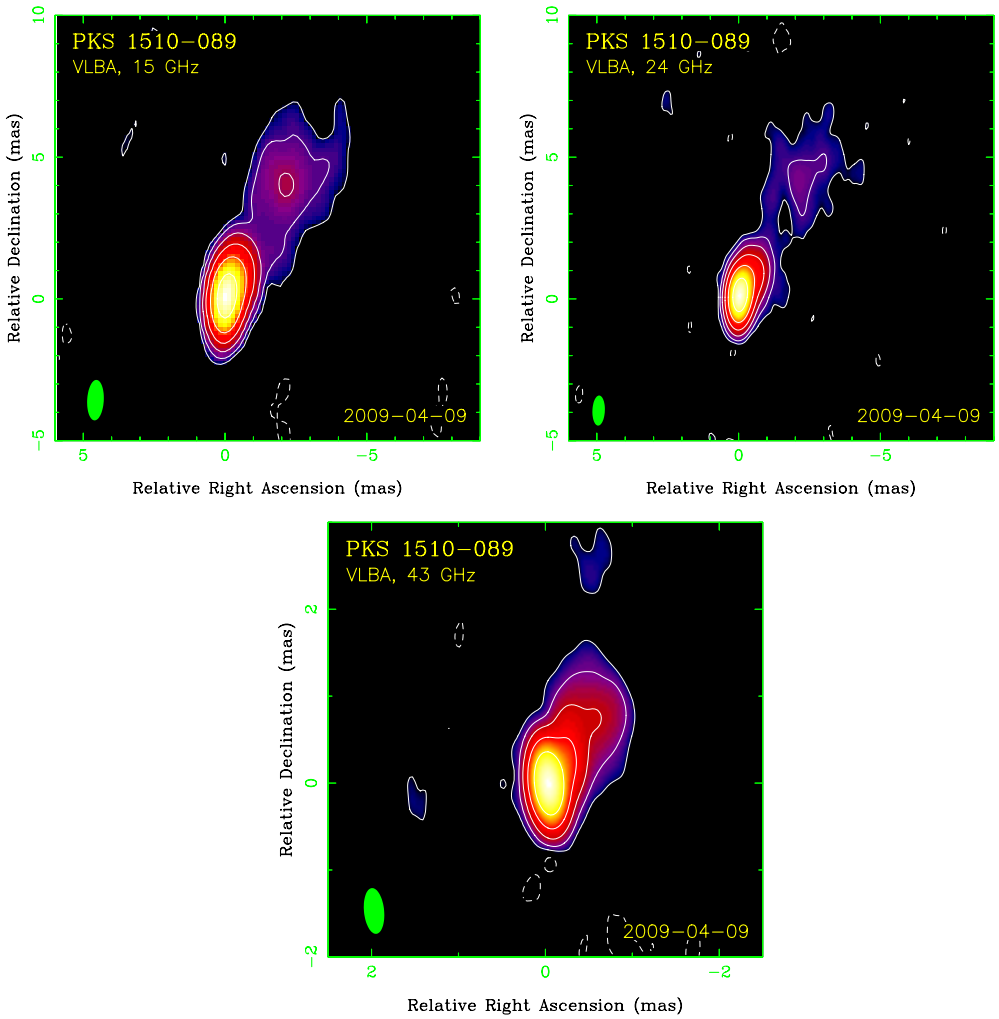

Figure 21. Stokes *I* CLEAN images of PKS 1510-089 observed by VLBA on 2009 April 9, at 15, 24, and 43 GHz. The lowest contour and peak intensity are 0.7 mJy beam^{-1} and 1.47 Jy beam^{-1} (15 GHz), 0.7 mJy beam^{-1} and 1.56 Jy beam^{-1} (24 GHz), and 2 mJy beam^{-1} and 1.85 Jy beam^{-1} (43 GHz). Contours are plotted with a step ×4. Natural weighting of visibility data is used, half-power beamwidth (HPBW) beam size is shown in the lower left corner. Angular size of 1 mas corresponds to 5 pc.

(A color version of this figure is available in the online journal.)

The observed MW SEDs of PKS 1510-089, reported in Figure 24, show that during the flaring state, the IC peak dominated over the synchrotron one by more than 1 order of magnitude. Indeed, even if both the synchrotron and IC peak frequencies are not sampled in our data set, we can estimate their typical peak flux by extrapolating the LP best-fit model for the γ-ray data, and by fitting the radio, optical, and UV SED points by means of cubic function. In the case of the synchrotron component, simultaneous millimeter and optical/UV data indicate that the peak flux should not be higher than a few times 10^{-11} erg cm^{-2} s^{-1}. In the case of the IC component, since the spectrum is mildly curved with the peak energy below the threshold of our analysis (200 MeV), the peak flux must be a few times 10^{-10} erg cm^{-2} s^{-1}. The presence of a pronounced BBB and the Compton dominance of about 10, during the flaring states, suggest that the contribution from photons originating outside the jet is appropriate to model the broadband SED.

The absence of X-ray/γ-ray flux correlation hints that the ERC flux variations depend on a change in the high-energy spectral index of the electron distribution, instead of a change in the external radiation field. In Section 4.2, we noted that the lack of γ-ray/UV correlation suggests that BBB variations are excluded as a main driver of the γ-ray variability. We tested the change of electron distribution by studying the correlation between the logarithms of the γ-ray and of the optical R fluxes (see Figure 16). The relation between the γ-ray and optical flux, fitted by means of PL, returns an exponent of $\sim$0.5 (or $\sim$0.6 if we use the 13 day shifted optical light curve discussed in Section 4.2). Despite the large scatter, this value is very interesting, because synchrotron and IC fluxes correlate very differently in the case of SSC, ERC/BLR, and ERC/DT. Moreover, the correlation depends on the low- and high-energy range chosen, respectively, for the synchrotron and IC component (Katarzyński et al. 2005). To have an estimate of the PL exponent for this correlation, we reproduced numerically a set of SEDs comparable to that observed for PKS 1510-089, using a well-tested code (Tramacere 2007; Tramacere et al. 2009; Tramacere & Tosti 2003). We calculated an ERC-dominated model, where the γ-ray emission is dominated by the BLR contribution and the electron distribution is a BPL. We fixed all the parameters and we increased the high-energy index of the electron distribution from -3.5 to -2.5 to evaluate the correlation between the optical energy emission ($\nu F(\nu)$ at 10^{14} Hz) and the integrated $F(E > 200\,\mathrm{MeV})$ γ-ray flux, taking

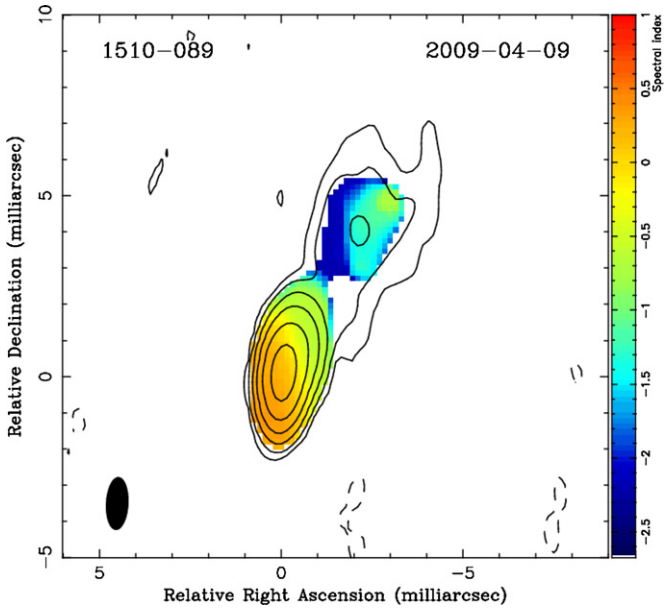

Figure 22. Spectral index s_r ($F(\nu) \propto \nu^{s_r}$) map between 15.4 and 23.8 GHz (shown in color) of PKS 1510-089 as observed by the VLBA on 2009 April 9. The overlaid contours represent total intensity at 15.4 GHz (see Figure 21 for details). The spectral index map was smoothed by a median filter with a 0.6 mas radius.

(A color version of this figure is available in the online journal.)

separately into account the three IC components SSC, ERC/BLR, and ERC/DT, as shown in Figure 25. The resulting flux relations were fitted by simple PLs and the resulting exponents were 3.1 for the SSC, 1.8 for ERC/DT, and 0.4 for ERC/BLR. The last one was the only one found to be consistent with that observed for PKS 1510-089 ($\simeq$ 0.5–0.6) and therefore, we can disfavor both SSC and ERC/DT.

The SEDs of the ERC/BLR model in the upper panel of Figure 25 have a curvature more pronounced than the ERC/DT ones. This is due to the KN cross section, because UV photons emitted from the accretion disk and reflected toward the jet by the BLR are blueshifted roughly by a factor of Γ. For $\Gamma \simeq 10$, the typical energy of these photons in the emitting region rest frame is then $\simeq 10^{16}$ Hz, hence the IC scattering with the electrons with $\gamma \simeq 1000$ occurs under a mild KN regime. The resulting smooth curvature has a value of $\simeq 0.1$ that is compatible with the observed one.

5.2. Spectral Energy Distribution Modeling and Jet Energetics

We attempt a leptonic ERC/BLR-oriented SED modeling. We aim to reproduce the SEDs for the three flares with simultaneous data from radio to γ-ray energies, namely, flares b, c, and d. Moreover, we try also to fit the quiescent state. Although variability timescales reached values of a fraction of day, LAT data required longer integration times to produce an SED enough good for spectral modeling. The intermediate fluxes of the synchrotron and BBB components, observed during the γ-ray integration period (red filled circles in Figure 24), are used in the fitting procedure as representative of the flare-averaged state of the low-energy bump.

Since the correlation between the γ-ray and the optical fluxes (see Section 5.1 and Figure 25) favors an ERC/BLR scenario, we assume that the dissipation zone is in the subparsec scale. This is also consistent with the mild curvature observed in the γ-ray spectra. Indeed, as shown in the previous section, the ERC/BLR process occurs under the KN regime leading to the curved MeV/GeV spectral shape that matches the one observed in the *Fermi* spectra.

We assume a jet viewing angle of $\theta = 2.^{\circ}5$ for both the flaring and the quiescent states. During the flaring states, we choose a bulk Lorentz factor in the range [14–16], resulting in a beaming factor range of [20–21.5] that is compatible with the VLBI observations. During the quiescent state, we use a bulk Lorentz factor of 12.0, corresponding to a beaming factor of about 18.8.

As a further step, we estimate the accretion disk physical characteristics using the UV data. We use the UV observations during the lowest synchrotron state of our data set as an estimate for the upper limit of the accretion disk luminosity

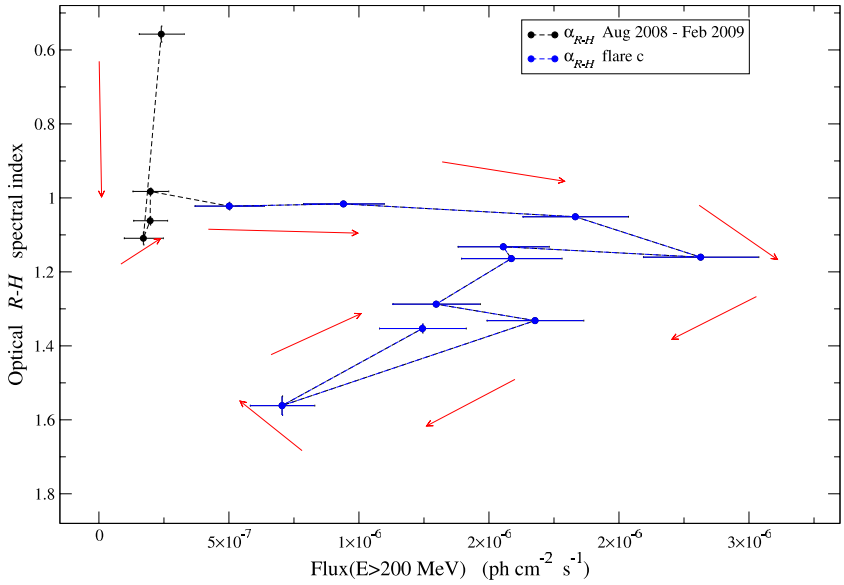

Figure 23. Optical $R-H$ spectral index vs. the LAT Flux above 200 MeV. The black points refer to the 2008 August to 2009 February period, and are too poorly sampled to be used for investigating the optical/γ-ray connection. The blue points overlap mainly the flare c, in particular the subflare peaking at about MJD 54909 (see Figure 2, panel (d)). The red arrows shows the chronological sequence.

(A color version of this figure is available in the online journal.)

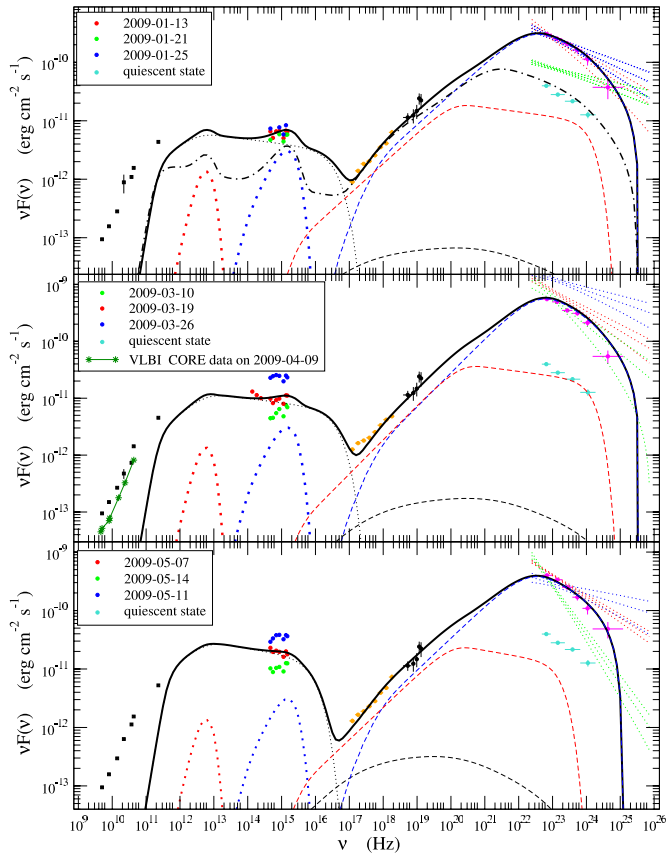

Figure 24. Red solid circles correspond to simultaneous optical/UV data representing the intermediate state during the γ-ray integration period. Blue and green circles correspond to the highest and lowest flux states, respectively, observed during the same integration period. The *Swift*-XRT data (orange points) are integrated during the same interval of the LAT data, and the *Swift*-BAT data represent the five year fluxes discussed in Section 4.1. The black squares represent GASP radio data, integrated during the flares. The cyan points correspond to the LAT quiescent state SED. The magenta points represent the γ-ray SED integrated during the flare. The blue, green, and red dotted lines represent the PL best fit of the γ-ray data, for a daily integration and simultaneous to the optical/UV data with the same color. The thin black dotted line represents the flaring synchrotron emission. The thin black dashed line corresponds to flaring SSC emission. The red and blue thick dotted lines correspond to the dusty torus and BBB emission, respectively. The red and blue thin dashed lines correspond to the ERC/DT and ERC/BLR flaring emission, respectively. The solid black thick line represents the sum of all the flaring model components. The thick dot-dashed line represents the sum of all the model components for the quiescent state alone.

(A color version of this figure is available in the online journal.)

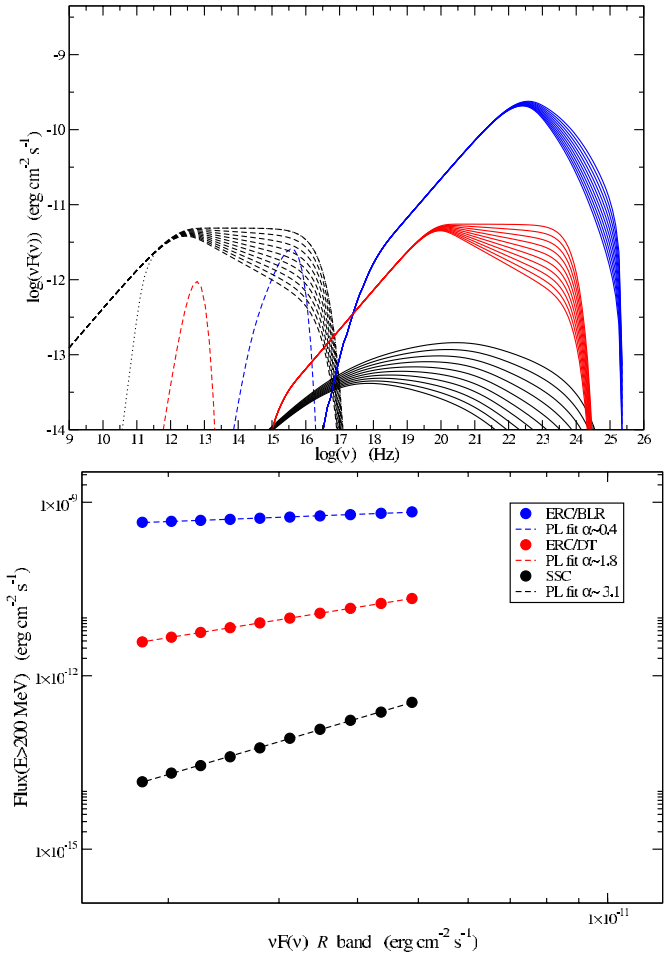

Figure 25. Upper panel: the SEDs for the different values of the high-energy electron distribution index. The black dashed lines represent the synchrotron emission without self-absorption. The black dotted line represents the synchrotron self-adsorbed emission. The black solid lines correspond to SSC emission. The red and blue dotted lines correspond to the dusty torus and BBB emission, respectively. The red and blue solid lines correspond to the ERC/DT and ERC/BLR emission, respectively. Lower panel: optical/γ-ray flux correlations for ERC/BLR (blue solid circles), ERC/DT (red solid circles), and SSC (black solid circles); dashed lines are the power-law relations.

(A color version of this figure is available in the online journal.)

(L_d). According to the observed UV flux and to the luminosity distance, we set a reference value of $L_d \simeq 3 \times 10^{45}$ erg s^{-1}. We model the accretion disk, following the prescription in King (2008) and rearranging the expression as in Ghisellini et al. (2009), using a multi-temperature blackbody with a temperature profile given by

$$T^4_{\rm disk}(R) = \frac{3R_S L_d}{16\pi\epsilon\sigma_{\rm SB}R^3}\left[1-\left(\frac{3R_S}{R}\right)^{1/2}\right], \qquad (2)$$

where $\sigma_{\rm SB}$ is the Stefan–Boltzmann constant, $R_S = 2\,GM_{\rm BH}/c^2$ is the Schwarzschild radius for a BH mass $M_{\rm BH}$, $3R_S$ is the last stable orbit in the case of Schwarzschild BH, and ϵ is the accretion efficiency that is linked to the bolometric luminosity and to the accretion mass rate $\dot{M}$, by $L_d = \epsilon\dot{M}c^2$. We assume that the radiative region of the disk extends from $\simeq 3R_S$ to $\simeq 500R_S$. Since $T_{\rm disk}(R)$ peaks at $R \simeq 4R_S$, we can use the UV data to constrain the peak of $T_{\rm diks}(R)$ and we can use Equation (2) to estimate R_S. From our data, we get a value of $T^{\rm peak}_{\rm disk} \simeq 4 \times 10^4$ K. Assuming as a reference value for the accretion efficiency $\epsilon \simeq 0.1$, we get $R_S \simeq 1.6 \times 10^{14}$ cm. The BH mass $M_{\rm BH}$ is then about $5.4 \times 10^8\,M_\odot$ and the accretion rate of about $0.5\,M_\odot$ yr^{-1} that corresponds to $\simeq 0.04$ times the Eddington accretion rate ($\dot{M}_{\rm Edd}$). The value of the BH mass estimated from our UV data is compatible with that obtained by Oshlack et al. (2002) using the virial assumption with measurements of the Hβ FWHM and luminosity ($M_{\rm BH} \simeq 3.9 \times 10^8\,M_\odot$), and by Xie et al. (2005; $M_{\rm BH} \simeq 2 \times 10^8\,M_\odot$).

The radius of the BLR can be estimated using the empirical relation by Kaspi et al. (2005) and Bentz et al. (2006):

$$R_{\rm BLR} \simeq 20\left[\frac{\nu^* L(\nu^*)}{10^{44}\,{\rm erg\,s^{-1}}}\right]^{0.5}\ {\rm lt\text{-}days}, \qquad (3)$$

where $\nu^* \simeq 5.878 \times 10^{14}$ Hz. According to the UVOT data, we estimate $\nu^* L(\nu^*) < 2 \times 10^{45}$ erg s^{-1}, and we get a value of $R_{\rm BLR} < 2.3 \times 10^{17}$ cm. We use BLR radius of about 1.6×10^{17} cm with reflectivity value of 0.1 (Ghisellini et al.

Table 5
Best-fit Parameters for the SED Modeling in the Case of BKN Electron Distribution

Flare	L_D (10^{45} erg s^{-1})	$M_{\rm BH}$ ($10^8 M_\odot$)	$R_{\rm BLR}$ (10^{17} cm)	$R_{\rm DT}$ (10^{17} cm)	Γ	$R_{\rm rad}$ (10^{17} cm)	B (G)	N_e No./cm^3	$\gamma_{\rm min}$	$\gamma_{\rm max}$	$\gamma_{\rm br}$	p	p_1
b	3.0	5.6	1.6	12.0	14.0	0.32	1.0	550	1.0	2.2×10^4	220	1.95	3.15
c	...	...	...	...	15.5	0.32	1.1	300	1.0	2.2×10^4	280	1.80	3.15
d	...	...	...	...	16.0	0.25	2.2	800	1.0	7.0×10^3	200	1.90	3.20
Quiescent	...	...	...	...	12.0	0.43	1.0	350	1.0	2.2×10^4	65	1.95	3.20

Note. $R_{\rm diss} < R_{\rm BLR}$, $R_{\rm diss} < R_{\rm DT}$, $T_{\rm disk}^{\rm peak} = 4 \times 10^4$ K, $T_{\rm DT} = 100$ K, and $\theta = 2^\circ.5$.

Table 6
Jet Power for the Case of BKN Modeling

Flare	$L_{\rm jet}$ (10^{45} erg s^{-1})	$L_{\rm rad}$ (10^{45} erg s^{-1})	$L_e/L_{\rm jet}$	$L_B/L_{\rm jet}$	$L_{\rm rad}/L_{\rm jet}$	U'_e (erg cm^{-3})	U'_e/U'_B	$L_{\rm jet}/L_D$
b	2.32	0.26	0.025	0.316	0.112	0.0031	0.08	0.77
c	2.17	0.46	0.027	0.502	0.211	0.0026	0.05	0.72
d	4.83	0.34	0.016	0.606	0.078	0.0049	0.03	1.61
Quiescent	2.31	0.07	0.016	0.423	0.031	0.0015	0.04	0.77

2009). The DT is modeled as a BB with a temperature $T_{\rm DT}$ of about 100 K, and a reflectivity of 0.3 (Ghisellini et al. 2009). The distance is set to a typical value of $\simeq 10^{18}$ cm, and it is fine tuned in the fit in order that the BLR/DT+BLR/ERC correctly match the X-ray and hard X-ray data.

We use an emitting region size ($R_{\rm rad}$) in the range [2–5] $\times$ 10^{16} cm that is almost twice the value estimated from the fast variability. In this regard, we note that since we are describing flare-averaged states, with integration times of the order of a few weeks, the discrepancy with the fast variability estimate is not problematic. As electron energy distribution $N(\gamma)$ we use a BPL:

$$N(\gamma) \propto \begin{cases} \gamma^{-p} & \text{for} \quad \gamma_{\rm min} \leqslant \gamma < \gamma_{br} \\ \gamma^{-p1} & \text{for} \quad \gamma_{br} \leqslant \gamma \leqslant \gamma_{\rm max} \end{cases} \tag{4}$$

with the number density of the electrons

$$N_e = \int_{\gamma_{\rm min}}^{\gamma_{\rm max}} N(\gamma) d\gamma. \tag{5}$$

The low-energy spectral index (p) is chosen $\simeq 1.9$, as hinted by the typical X-ray photon index (see Section 5.1); the value of the break energy ($\gamma_{\rm br}$) is chosen to match the position of the peak energy of the IC bump. It is of the order of [250–300] and it is tuned in the three flares to fit the data. The high-energy spectral index (p_1) is chosen according to the average spectral index of the LAT data, and the reference value is $\simeq 3$. Magnetic field intensity B is chosen to be 1.0 G for flares b and c, while for the flare d we need to use a larger value of B and a more compact region size.

All the flares are assumed to occur at dissipation distance from the disk ($R_{\rm diss}$) that is within the BLR and the DT ($R_{\rm diss} < R_{\rm BLR}$, $R_{\rm diss} < R_{\rm DT}$). The resulting best fit of the MW SEDs is reported in Figure 24, and the corresponding values of the best-fit parameters for the three flares are reported in Table 5.

To have an indication of the change in the energetic contents of the jet as a function of the flaring activity, we try to fit also the quiescent γ-ray SED. Considering the lack of MW data during this time interval, we assume that the X-ray SED is close to the state observed during flare b, as supported by the low X-ray variability. From the MW light curves reported in Figure 7, we infer that the optical/UV flux is at a level of few times 10^{-12} erg cm^{-2} s^{-1}. We can have an acceptable description of the MW SED during the quiescent γ-ray period using parameters comparable to those chosen for the flare b, but we need to decrease significantly $\gamma_{\rm br}$ to $\simeq 65$. The best-fit model is represented by the black dash-dotted line in the top panel of Figure 24.

It is interesting to study the evolution of the energetic content of the jet resulting from the SED modeling discussed above. We evaluate the total kinetic power of the jet as

$$L_{\rm jet} = \pi R_{\rm rad}^2 c \Gamma^2 (U'_e + U'_B + U'_p), \tag{6}$$

where the rest-frame magnetic energy density is given by $U'_B = B^2/8\pi$, the electron energy density is U'_e,[86] and $U'_p = 0.1 N_e m_p c^2$ is the cold-proton energy density, assuming that we have 1 cold proton per 10 electrons (Sikora et al. 2009). The power carried by the jet in terms of radiation is given by $L_{\rm rad} \simeq L' \Gamma^2/4$. We evaluate L' summing up the numerical integration of each radiative component (synchrotron, SSC, ERC/BLR, ERC/DT) as observed in the jet rest frame. In Table 6, we report the results for flares b, c, and d and the quiescent state, corresponding to the physical parameters reported in Table 5.

The total kinetic power of the jets is almost steady, except during the flare d when it increased by a factor of two. Indeed, for the case of flares b and c, we find values of $L_{\rm jet}$ that are comparable with that of the quiescent state. In contrast, we note that the value of the electron energy density during all the flaring states is much larger than that estimated during the quiescent state, and, during the flare d, it increased with respect to the quiescent state by about a factor of 2.7. The low values of U'_e/U'_B reflect the low SSC contribution. Indeed, for the choice of our model parameters, the SSC is always negligible compared to the other radiative components. As final remark, we note that the radiative efficiency of the jet ($L_{\rm rad}/L_{\rm jet}$), is $\simeq 0.03$ during the quiescent state, and increases up to $\simeq 0.2$ during flare c.

We now compare the jet total kinetic luminosity with the accretion disk luminosity. According to the analysis reported in Ghisellini et al. (2010), if the jet power comes from the accretion process, then the accreting mass has to account both for the disk

[86] $U'_e = \int_{\gamma_{\rm min}}^{\gamma_{\rm max}} \gamma m_e c^2 N(\gamma) \frac{1}{2} d\gamma$.

luminosity and for jet power. We can write

$$\epsilon_{\rm tot}\dot{M}c^2 = \epsilon_D\dot{M}c^2 + \epsilon_{\rm jet}\dot{M}c^2. \quad (7)$$

The ratio of $L_{\rm jet}$ to L_D, reported in Table 6 is equal to $\epsilon_{\rm jet}/\epsilon_D$. Using as ϵ_D the typical value of 0.1, we need a total efficiency $\epsilon_{\rm tot} \gtrsim 0.26$ that is still compatible with the maximum efficiency in the case of a Kerr BH.

5.3. Comparison with Other Fermi-LAT FSRQs

It is interesting to compare the flaring activity of PKS 1510-089 with other FSRQs observed by *Fermi*. 3C 454.3 ($z = 0.859$), reached an isotropic luminosity above 100 MeV $L(E > 100) \simeq 8 \times 10^{48}$ erg s^{-1} during the period of 2008 August/September (Abdo et al. 2009a). It became the highest ever recorded object in the gamma rays during the flare in 2009 December (Escande & Tanaka 2009), with a luminosity $L(E > 100) \simeq 1 \times 10^{49}$ erg s^{-1}, about five times larger than the maximum flare resolved luminosity of PKS 1510-089. The source during the flares exhibited rapid variability down to sub-daily timescales that is comparable to that observed in PKS 1510-089. The γ-ray spectra of 3C 454.3 object show a spectral break around 2 GeV (Abdo et al. 2009a). In this case, we see a relevant difference with respect to PKS 1510-089 that exhibited a mild curvature spectrum. A possible reason, as explained in the previous section, is that in the case of 3C 454.3 the dominant external photon field originates in the DT and not in the BBB. Thus, the IC process occurs under the TH regime, and the break reflects the break in the electron distribution. The BH mass is estimated to be $M_{\rm BH} \simeq 4 \times 10^9\ M_\odot$, and the disk luminosity of the order of $L_D \simeq 2 \times 10^{46}$ erg s^{-1}, both these values are 1 order of magnitude larger than PKS 1510-089. Another interesting difference is that the 3C 454.3 exhibits no BBB features during the high optical and γ-ray outburst.

The FSRQ PKS 1502+106 ($z = 1.839$), during the outburst in 2008 August (Abdo et al. 2010b), reached a luminosity $L \simeq 1 \times 10^{49}$ erg s^{-1}, showing a very large Compton dominance up to 100. As in the case of 3C 454.3, this object exhibited no BBB feature at UV energies. The flare of this object was an isolated episode, rather than a flaring sequence. The γ-ray spectrum showed a curved shape, similar to PKS 1510-089, during the full integration period, and during the post-flare state. The curvature values, 0.1–0.2, are comparable to those observed in PKS 1510-089, hence also in this case an origin in the KN effect is possible, as well as a curved electron distribution with the IC process in TH regime. The MW variability of this object is very different from that observed in PKS 1510-089. Indeed, the X-ray flux followed both the γ-ray and the optical flux. Moreover, there was a strong correlation between the UV and the γ-ray. Probably this can be explained with a sharp change in the density of the radiating electrons, or in the beaming factor.

PKS 1454-354 ($z = 1.424$), another distant FSRQs discovered in the γ-ray by *Fermi* during the 2008 August/September flaring activity (Abdo et al. 2009b), reached a luminosity $L(E > 100) \simeq 7 \times 10^{48}$ erg s^{-1}, and exhibited a rapid variability with hours/days timescales.

We conclude that the most rapid timescale for the γ-ray variability (down to 6/12 hr) is common to this class of objects, despite the bolometric γ-ray luminosity. This timescale is limited by the minimum LAT integration time required to extract a flux for object with $F(E > 200$ MeV) of the order of 10^{-5} photons cm^{-2} s^{-1}, hence a faster variability could be possible. Compared to those listed above, PKS 1510-089 seems to be a less powerful object in terms of both γ-ray luminosity and thermal luminosity. The curvature in the γ-ray spectrum, when compared to the spectral break observed in other sources such as 3C 454.3, may be understood as a signature of the KN regime, hence of a dissipation region within the BLR.

6. CONCLUSIONS

We presented MW observations of PKS 1510-089 during a period of about 11 months, when the source exhibited a strong evolution of its broadband SED, characterized by a complex variability both at optical/UV and γ-ray energies, with timescales detected down to the level of 6/12 hr. The γ-ray flux shows the usual harder when brighter trend, for flux levels of $F(E > 0.2\,{\rm GeV}) \gtrsim 2.4 \times 10^{-7}$ photons cm^{-2} s^{-1}. For lower flux levels, the trend seems to be the opposite, but the low statistics during these dimmer states does not allow us to give a purely physical interpretation. The spectrum shows a mild curvature, both during the flares and during the full-period integration, well described by an LP law, and can be understood as a signature of the KN effect.

The γ-ray flux shows a complex correlation with the other wavelengths. There is no correlation at all with the X-ray band, a week correlation with the UV, and a strong correlation with the optical (R) flux. Thanks to the unprecedented continuous LAT γ-ray sky survey, we were able to find a lag in the γ-ray light curve, with the γ-ray band leading the R band by about 13 days. Because of this complex multi-band variability, we assume that a change in the beaming factor cannot account for the flaring activity of this object. Indeed, assuming as the main driver a change in the beaming factor, we would expect at least a weak correlation between the X-ray and the optical band, or between the X-ray and the γ-ray. This is also in agreement with the absence of correlation between the jet kinematic power($L_{\rm jet}$) and the flaring episodes observed in our data set.

UV data allowed us to estimate the mass of the BH of $\simeq 5.6 \times 10^8\ M_\odot$. This value, that is in agreement with other estimates based on different methods, is smaller compared to the very luminous and distant FSRQs, with BH masses of the order of $10^9\ M_\odot$. As a consequence of the estimated BH mass and thermal component luminosity, the accretion rate of $\simeq 0.04\ \dot{M}_{\rm Edd}$ is also lower when compared to the expectation in the case of FSRQs ($\simeq 0.1\ \dot{M}_{\rm Edd}$). Due to the low redshift of the source, the bolometric isotropic γ-ray luminosity is also smaller compared to other distant FSRQs observed by *Fermi*. Indeed, PKS 1510-089 has a typical γ-ray luminosity and BH mass about 1 order of magnitude lower compared to sources like 3C 454.3 or PKS 1502-106.

Despite the relatively lower power in the thermal and non-thermal outputs, PKS 1510-089 exhibits a quite large Compton dominance, as observed in the most powerful FSRQs, and prominent a BBB signature. The object could be a representative of an aged FSRQ, hence the analysis here presented is relevant in order to understand the evolution of these objects.

We note the puzzling feature of the BBB UV shape. The BBB was still prominent during the historical maximum optical state during 2009 May, although the optical/UV spectral index was softer compared to that in the quiescent state.

The analysis presented here shows the importance of the MW monitoring of blazars, independent of the γ-ray triggering. Indeed, only by comparing the flaring and quiescent states, and understanding the evolution of the physical parameters as a function of the flaring activity, is it possible to discriminate among the possible physical scenarios.

The *Fermi*-LAT Collaboration acknowledges the generous support of a number of agencies and institutes that have supported the *Fermi*-LAT Collaboration. These include the National Aeronautics and Space Administration and the Department of Energy in the United States, the Commissariat à l'Energie Atomique and the Centre National de la Recherche Scientifique/Institut National de Physique Nucléaire et de Physique des Particules in France, the Agenzia Spaziale Italiana and the Istituto Nazionale di Fisica Nucleare in Italy, the Ministry of Education, Culture, Sports, Science and Technology (MEXT), the High Energy Accelerator Research Organization (KEK) and the Japan Aerospace Exploration Agency (JAXA) in Japan, and the K. A. Wallenberg Foundation, the Swedish Research Council, and the Swedish National Space Board in Sweden. Additional support for science analysis during the operations phase is gratefully acknowledged from the Istituto Nazionale di Astrofisica in Italy and the Centre National d'Études Spatiales in France.

Part of this work is based on archival data and on bibliographic information obtained from the NASA/IPAC Extragalactic Database (NED).

This paper is partly based on observations carried out at the German-Spanish Calar Alto Observatory, which is jointly operated by the MPIA and the IAA-CSIC.

Acquisition of the MAPCAT data is supported in part by the Spanish Ministry of Science and Innovation and the Regional Government of Andalucía through grants AYA2007-67626-C03-03 and P09-FQM-4784, respectively.

This work was partly supported by the Italian Space Agency through contract ASI-INAF I/088/06/0 for the Study of High-Energy Astrophysics. St. Petersburg University team acknowledges support from Russian RFBR foundation via grant 09-02-00092. AZT-24 observations are made within an agreement between Pulkovo, Rome, and Teramo observatories.

Abastumani Observatory team acknowledges financial support by the Georgian National Science Foundation through grant GNSF/ST08/4-404.

The research at Boston University (BU) was funded in part by NASA Fermi Guest Investigator grants NNX08AV65G and NNX08AV61G, and by the National Science Foundation (NSF) through grant AST-0907893.The PRISM camera at the Perkins Telescope of Lowell Observatory was developed by K. Janes et al. at BU and Lowell Observatory, with funding from the NSF, BU, and Lowell Observatory. The Liverpool Telescope is operated on the island of La Palma by Liverpool John Moores University in the Spanish Observatorio del Roque de los Muchachos of the Instituto de Astrofisica de Canarias, with funding from the UK Science and Technology Facilities Council.

This research has made use of observations from the MOJAVE database that is maintained by the MOJAVE team (Lister et al. 2009b). The MOJAVE project is supported under National Science Foundation grant 0807860-AST and NASA-Fermi grant NNX08AV67G.

The Lebedev Physical Institute team was partly supported by the Russian Foundation for Basic Research (project 08-02-00545). K.S. was supported by stipend from the IMPRS for Astronomy and Astrophysics. We thank A. P. Marscher and S. Jorstad for providing multi-wavelength data.

The VLBA is a facility of the National Science Foundation operated by the National Radio Astronomy Observatory under cooperative agreement with Associated Universities, Inc.

Facilities: Fermi (LAT), *Swift* (XRT, UVOT), WEBT, VLBA.

REFERENCES

Abdo, A. A., et al. 2009a, ApJ, 699, 817
Abdo, A. A., et al. 2009b, ApJ, 697, 934
Abdo, A. A., et al. 2010a, ApJS, 188, 405
Abdo, A. A., et al. 2010b, ApJ, 710, 810
Abdo, A. A., et al. 2010c, ApJ, 710, 1271
Abdo, A. A., et al. 2010d, ApJ, in press (arXiv:1004.0348)
Ajello, M., et al. 2008, ApJ, 673, 96
Ajello, M., et al. 2009a, ApJ, 699, 603
Ajello, M., et al. 2009b, ApJ, 690, 367
Atwood, W. B., et al. 2009, ApJ, 697, 1071
Bentz, M. C., Peterson, B. M., Pogge, R. W., Vestergaard, M., & Onken, C. A. 2006, ApJ, 644, 133
Bessell, M. S., Castelli, F., & Plez, B. 1998, A&A, 333, 231
Burrows, D. N., et al. 2005, Space Sci. Rev., 120, 165
Cardelli, J. A., Clayton, G. C., & Mathis, J. S. 1989, ApJ, 345, 245
Cash, W. 1979, ApJ, 228, 939
Ciprini, S., & Corbel, S. 2009, ATel, 1897
Cutini, S., & Hays, E. 2009, ATel, 2033
D'Ammando, F., et al. 2008, ATel, 1436
D'Ammando, F., et al. 2009a, A&A, 508, 181
D'Ammando, F., et al. 2009b, ATel, 1957
Dermer, C. D., & Schlickeiser, R. 2002, ApJ, 575, 667
Escande, L., & Tanaka, Y. T. 2009, ATel, 2328, 1
Gehrels, N., et al. 2004, ApJ, 611, 1005
Ghisellini, G., & Maraschi, L. 1989, ApJ, 340, 181
Ghisellini, G., Tavecchio, F., Foschini, L., Ghirlanda, G., Maraschi, L., & Celotti, A. 2010, MNRAS, 402, 497
Ghisellini, G., Tavecchio, F., & Ghirlanda, G. 2009, MNRAS, 399, 2041
Giommi, P., et al. 2006, A&A, 456, 911
Hartman, R. C., et al. 1999, ApJS, 123, 79
Homan, D. C., Wardle, J. F. C., Cheung, C. C., Roberts, D. H., & Attridge, J. M. 2002, ApJ, 580, 742
Hovatta, T., Valtaoja, E., Tornikoski, M., & Lähteenmäki, A. 2009, A&A, 494, 527
Jones, T. W., O'dell, S. L., & Stein, W. A. 1974, ApJ, 188, 353
Kaspi, S., Maoz, D., Netzer, H., Peterson, B. M., Vestergaard, M., & Jannuzi, B. T. 2005, ApJ, 629, 61
Kataoka, J., et al. 2008, ApJ, 672, 787
Katarzyński, K., Ghisellini, G., Tavecchio, F., Maraschi, L., Fossati, G., & Mastichiadis, A. 2005, A&A, 433, 479
King, A. 2008, New Astron. Rev., 52, 253
Komatsu, E., et al. 2009, ApJS, 180, 330
Kovalev, Y. Y., et al. 2009, ApJ, 696, L17
Krimm, H. A., et al. 2009, ATel, 1963
Landau, R., et al. 1986, ApJ, 308, 78
Larionov, V. M., Konstantinova, T. S., & Blinov, D. A. 2009a, ATel, 2045
Larionov, V. M., et al. 2009b, ATel, 1990
Lister, M. L., Homan, D. C., Kadler, M., Kellermann, K. I., Kovalev, Y. Y., Ros, E., Savolainen, T., & Zensus, J. A. 2009a, ApJ, 696, L22
Lister, M. L., et al. 2009b, AJ, 137, 3718
Lister, M. L., et al. 2009c, AJ, 138, 1874
Lockman, F. J., & Savage, B. D. 1995, ApJS, 97, 1
Madejski, G., Takahashi, T., Tashiro, M., Kubo, H., Hartman, R., Kallman, T., & Sikora, M. 1996, ApJ, 459, 156
Maraschi, L., Ghisellini, G., & Celotti, A. 1992, ApJ, 397, L5
Marscher, A. P., et al. 2010a, ApJ, 710, L126
Marscher, A. P., et al. 2010b, arXiv:1002.0806
Massaro, E., Perri, M., Giommi, P., & Nesci, R. 2004, A&A, 413, 489
Mattox, J. R., et al. 1993, ApJ, 410, 609
Mattox, J. R., et al. 1996, ApJ, 461, 396
Nandikotkur, G., Jahoda, K. M., Hartman, R. C., Mukherjee, R., Sreekumar, P., Bottcher, M., Sambruna, R. M., & Swank, J. H. 2007, ApJ, 657, 706
Oshlack, A. Y. K. N., Webster, R. L., & Whiting, M. T. 2002, ApJ, 576, 81
Page, K. L., Reeves, J. N., O'Brien, P. T., & Turner, M. J. L. 2005, MNRAS, 364, 195
Poole, T. S., et al. 2008, MNRAS, 383, 627
Pucella, G., et al. 2008, A&A, 491, L21
Pucella, G., et al. 2009, ATel, 1968
Raiteri, C. M., Villata, M., Lanteri, L., Cavallone, M., & Sobrito, G. 1998, A&AS, 130, 495
Ritz, S. 2007, in AIP Conf. Proc. 921, The First GLAST Symp., ed. S. Ritz, P. Michelson, & C. A. Meegan (Melville, NY: AIP), 3
Rybicki, G. B., & Lightman, A. P. 1979, Radiative Processes in Astrophysics (New York: Wiley-Interscience)

Schlegel, D. J., Finkbeiner, D. P., & Davis, M. 1998, ApJ, 500, 525
Sikora, M., Baejowski, M., Moderski, R., & Madejski, G. M. 2002, ApJ, 577, 78
Sikora, M., Begelman, M. C., & Rees, M. J. 1994, ApJ, 421, 153
Sikora, M., Stawarz, U., Moderski, R., Nalewajko, K., & Madejski, G. M. 2009, ApJ, 704, 38
Sokolovsky, K. V., Kovalev, Y. Y., Lobanov, A. P., Savolainen, T., Pushkarev, A. B., & Kadler, M. 2010, arXiv:1001.2591
Tadhunter, C. N., Morganti, R., Di Serego-Alighieri, S., Fosbury, R. A. E., & Danziger, I. J. 1993, MNRAS, 263, 999
Thompson, D. J., Djorgovski, S., & De Carvalho, R. 1990, PASP, 102, 1235
Tramacere, A. 2007, PhD thesis, La Sapienza Univ.
Tramacere, A. 2008, ATel, 1743
Tramacere, A., Giommi, P., Perri, M., Verrecchia, F., & Tosti, G. 2009, A&A, 501, 879
Tramacere, A., & Tosti, G. 2003, New Astron. Rev., 47, 697
Vercellone, S., et al. 2009, ATel, 1976
Villata, M., et al. 2006, A&A, 453, 817
Villata, M., et al. 2008, A&A, 481, L79
Villata, M., et al. 2009a, ATel, 1988
Villata, M., et al. 2009b, A&A, 504, L9
Xie, G. Z., Liu, H. T., Cha, G. W., Zhou, S. B., Ma, L., Xie, Z. H., & Chen, L. E. 2005, AJ, 130, 2506